



HAL
open science

Unraveling the Atomic Structure of Bulk Binary Ga–Te Glasses with Surprising Nanotectonic Features for Phase-Change Memory Applications

Maria Bokova, Andrey Tverjanovich, Chris J Benmore, Daniele Fontanari, Anton Sokolov, Maxim Khomenko, Mohammad Kassem, Ilya Ozheredov, Eugene Bychkov

► To cite this version:

Maria Bokova, Andrey Tverjanovich, Chris J Benmore, Daniele Fontanari, Anton Sokolov, et al.. Unraveling the Atomic Structure of Bulk Binary Ga–Te Glasses with Surprising Nanotectonic Features for Phase-Change Memory Applications. *ACS Applied Materials & Interfaces*, 2021, 13 (31), pp.37363 - 37379. 10.1021/acsami.1c09070 . hal-04217817

HAL Id: hal-04217817

<https://ulco.hal.science/hal-04217817>

Submitted on 26 Sep 2023

HAL is a multi-disciplinary open access archive for the deposit and dissemination of scientific research documents, whether they are published or not. The documents may come from teaching and research institutions in France or abroad, or from public or private research centers.

L'archive ouverte pluridisciplinaire **HAL**, est destinée au dépôt et à la diffusion de documents scientifiques de niveau recherche, publiés ou non, émanant des établissements d'enseignement et de recherche français ou étrangers, des laboratoires publics ou privés.

Unraveling the Atomic Structure of Bulk Binary Ga–Te Glasses with Surprising Nanotectonic Features for Phase-Change Memory Applications

Maria Bokova, Andrey Tverjanovich, Chris J. Benmore, Daniele Fontanari, Anton Sokolov, Maxim Khomenko, Mohammad Kassem, Ilya Ozheredov, and Eugene Bychkov*

Cite This: *ACS Appl. Mater. Interfaces* 2021, 13, 37363–37379

Read Online

ACCESS |

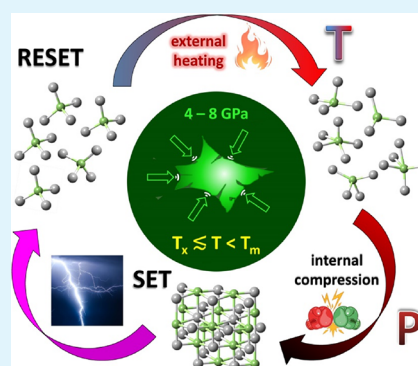
Metrics & More

Article Recommendations

Supporting Information

ABSTRACT: Binary Ge–Te and ternary Ge–Sb–Te systems belong to flagship phase-change materials (PCMs) and are used in nonvolatile memory applications and neuromorphic computing. The working temperatures of these PCMs are limited by low- T glass transition and crystallization phenomena. Promising high- T PCMs may include gallium tellurides; however, the atomic structure and transformation processes for amorphous Ga–Te binaries are simply missing. Using high-energy X-ray diffraction and Raman spectroscopy supported by first-principles simulations, we elucidate the short- and intermediate-range order in bulk glassy $\text{Ga}_x\text{Te}_{1-x}$, $0.17 \leq x \leq 0.25$, following their thermal, electric, and optical properties, revealing a semiconductor–metal transition above melting. We also show that a phase change in binary Ga–Te is characterized by a very unusual nanotectonic compression with the high internal transition pressure reaching 4–8 GPa, which appears to be beneficial for PCM applications increasing optical and electrical contrast between the SET and RESET states and decreasing power consumption.

KEYWORDS: phase-change materials, Ga–Te binaries, nanotectonic compression, first-principles simulations, X-ray diffraction, Raman spectroscopy, optical and electronic properties



INTRODUCTION

Germanium–tellurium binary and ternary phase-change materials (PCMs) belong to flagship PCMs and are widely used for optical storage and nonvolatile memory applications and recently for the development of brain-inspired computing technologies.^{1–5} The maximum working temperatures of the PCM elements of this type are limited by low- T glass transition and crystallization phenomena. Consequently, automotive and similar high- T applications need novel PCM systems capable of performing reliable temperature-resistant operation.^{6–8}

Gallium sesquitermelluride Ga_2Te_3 appears to be a promising high- T PCM characterized by low-power and ultrahigh-density memory applications.^{9,10} Deep insight into the structure and phase-change mechanism of Ga_2Te_3 requires a detailed knowledge of the Ga–Te system, in particular, of the corresponding binary glasses and liquids. $\text{Ga}_x\text{Te}_{1-x}$ glassy binaries were reported since 1963,¹¹ and the glass-forming region was found to be between $0.1 \leq x \leq 0.3$ for splat quenching and narrower for classical melt cooling.^{12–14} The thermal and electrical properties of glassy $\text{Ga}_x\text{Te}_{1-x}$ were extensively studied as well as switching phenomena and a semiconductor–metal transition under high pressure.^{12–17} Nevertheless, the structural studies are either missing (glasses) or controversial (liquids).^{18–20} In particular, X-ray diffraction

studies of liquid $\text{Ga}_x\text{Te}_{1-x}$ alloys over the entire composition range, $0 \leq x \leq 1$, have suggested a chemically ordered network but with a strong dissociation of Ga–Te units.¹⁸ As a result, the gallium local environment in stoichiometric L- Ga_2Te_3 was reported to be mixed: $N_{\text{Ga-X}} = N_{\text{Ga-Ga}} + N_{\text{Ga-Te}} = 1.9 + 1.6 = 3.5$. In contrast, the results of neutron diffraction with isotopic substitution and anomalous X-ray scattering at the Te K edge²⁰ have shown similar gallium local coordination, $N_{\text{Ga-Te}} = 3.5 \pm 0.5$, however, without a substantial number of Ga–Ga and Te–Te homopolar bonds. Finally, recent EXAFS studies of amorphous Ga_2Te_3 thin films, prepared by pulsed laser deposition and measured at the Ga and Te K edges, have revealed the tetrahedral gallium environment with a small fraction of Ga–Ga nearest neighbors (NNs), $N_{\text{Ga-X}} = N_{\text{Ga-Ga}} + N_{\text{Ga-Te}} = 0.21 + 3.79 = 4.00$.²¹ The results for Te-rich liquids, $x < 0.4$, are only approximate,^{18,19} roughly suggesting a tetrahedral gallium environment without further precision.

Received: May 16, 2021

Accepted: June 29, 2021

Published: July 28, 2021



Unraveling the atomic structure of bulk glassy Ga–Te alloys and following their electronic, optical, and transformation changes are the main goal of the present paper to establish the fundamental features required for the next generation of PCMs. High-energy X-ray diffraction supported by Raman spectroscopy and first-principles simulations is a highly efficient tool to solve this problem and will greatly advance our understanding of the phase-change mechanisms.

EXPERIMENTAL SECTION

Glass Synthesis. Bulk $\text{Ga}_x\text{Te}_{1-x}$ alloys, $0.17 \leq x \leq 0.25$, were prepared by classical melt quenching from high-purity elements Ga (99.999%, Neyco) and Te (99.999%, Cerac). The mixtures of 1 g were sealed in silica tubes (8 mm ID/10 mm OD) under vacuum (10^{-6} mbar). The batches were heated at a rate of $\approx 1 \text{ K min}^{-1}$ to 1250 K and homogenized at this temperature for a few days. The melts were then cooled down to 1050 K and quenched in ice/water. Mechanical milling (MM) was carried out using a planetary micromill Pulverisette 7 premium line (Fritsch GmbH, Germany) under an argon atmosphere. The MM- $\text{Ga}_{0.15}\text{Te}_{0.85}$ and MM- $\text{Ga}_{0.30}\text{Te}_{0.70}$ samples were prepared from 3 g of starting materials in the desired molar ratio introduced into a 45 mL zirconia jar along with 23 ZrO₂ grinding balls (10 mm in diameter). The ball-milling reaction lasted for 50 h at a speed of 320 rpm.

DSC Experiments. Glass characteristic temperatures, including the glass transition T_g and crystallization temperatures, were determined by differential scanning calorimetry (DSC) using a TA Instruments Q200 thermal analyzer. The samples of 5–10 mg were encapsulated in a sealed aluminum pan and heated at a rate of 10 K min^{-1} under a dry nitrogen atmosphere. Usually, three measurements were carried out for each $\text{Ga}_x\text{Te}_{1-x}$ composition to find the average glass transition temperature.

In Situ Temperature-Dependent X-ray Diffraction. In situ measurements of X-ray diffraction as a function of temperature were carried out under vacuum using a Rigaku Ultima IV high-resolution diffractometer equipped with a Rigaku SHT-1500 high-temperature camera and a sealed $\text{Co K}\alpha$ X-ray tube. The glass powder was placed in a platinum sample holder whose temperature was increased at a rate of 10 K min^{-1} . Above glass transition, the diffraction patterns were recorded every 10 K up to 643 K. After temperature measurements and cooling down the sample, the diffraction pattern was recorded again under ambient conditions.

Conductivity Measurements. The electrical transport of the samples was evaluated by ac conductivity measurements from room temperature to nearly a glass transition, $T_g - 30 \text{ K}$, using a Hewlett Packard 4194A impedance meter over the 100 Hz to 15 MHz frequency range. The as-prepared rectangular plates with a typical area of 6–8 mm² and a thickness of 0.4–0.6 mm were polished using SiC powder (9.3 μm grain size) and sputtered with gold on two opposite sides as electrodes. The sample resistance was determined using the complex impedance plots and converted into electrical conductivity using the geometrical factor (sample thickness and gold contact area).

Optical Absorption Experiments. The optical absorption of bulk glassy $\text{Ga}_{0.20}\text{Te}_{0.80}$ was studied using a polished plane-parallel plate with a thickness of 0.58 mm. A Shimadzu UV-3600 spectrophotometer was used for optical absorption measurements in the wavelength range of 0.8–3.2 μm . A far-IR region was covered by a Bruker Tensor FTIR spectrometer, allowing the extended IR range up to 25 μm . In addition, the two instruments have overlapping spectral domains between 2.5 and 3.2 μm .

Raman Spectroscopy Measurements. Raman spectra were measured at room temperature in backscattering geometry using a Senterra Raman spectrometer (Bruker) equipped with a microscope. The spectra were excited by a 785 nm laser diode with a power of 1 mW using a low magnification objective (10 \times , NA 0.25) to avoid laser-induced crystallization or damage of the glass samples and recorded in the 75–1500 cm^{-1} spectral range (reliable data above 100 cm^{-1}). The spectrometer resolution was 3 cm^{-1} .

High-Energy X-ray Diffraction. The 6-ID-D beamline at the Advanced Photon Source (Argonne National Laboratory, Chicago) was used for high-energy X-ray diffraction measurements in the top-up mode. The photon energy was 99.9758 keV, and the wavelength was 0.124014 Å. A two-dimensional (2D) setup was used for data collection with a Varex area detector, 2880 \times 2880 pixels, and a pixel size of 150 \times 150 μm^2 . The sample-to-detector distance was 287 mm. Cerium dioxide (CeO_2) was used as a calibrant. The exposure time was 0.1 s \times 3000 frames, using one dark-field image file followed by five light files. The sample image was saturated with a full beam; the attenuation was set to 0.1 for diffraction measurements. The 2D diffraction patterns were reduced using the Fit2D software.²² The measured background intensity was subtracted, and corrections were made for the different detector geometries and efficiencies, sample self-attenuation, and Compton scattering using standard procedures,²³ providing the X-ray structure factor $S_x(Q)$.

First-Principles Simulations. The DFT calculations of Raman spectra were carried out using Gaussian 16 software.²⁴ The structural optimization and harmonic vibrational frequency calculations were performed for size-limited clusters: GaTe_4H_4 , $\text{Ga}_2\text{Te}_2\text{H}_6$, $\text{Ga}_2\text{Te}_6\text{H}_4$, $\text{Ga}_3\text{Te}_8\text{H}_4$, $\text{Ga}_2\text{Te}_6\text{H}_6$, $\text{Ga}_2\text{Te}_5\text{H}_5$, Te_6 , and Te_8 . The Becke three-parameter hybrid exchange functional²⁵ and the Lee–Yang–Parr correlation functional (B3LYP)²⁶ were used for DFT simulations. The small-core relativistic pseudopotential basis set (cc-pVTZ-PP)²⁷ and the effective core potentials²⁸ were applied for cluster geometry optimization and Raman intensity calculations. Most of the structures were optimized using the tight convergence option, ensuring adequate convergence and reliability of computed wavenumbers. An extra quadratically convergent self-consistent field procedure²⁹ was used for difficult convergence cases. Further details of the DFT simulations are published elsewhere.^{30–32}

The Born–Oppenheimer molecular dynamics implemented within the CP2K package³³ was used for structural modeling of $\text{Ga}_{0.20}\text{Te}_{0.80}$. The generalized gradient approximation (GGA) and the PBE0 hybrid^{34,35} exchange–correlation functional combining the exact Hartree–Fock and density functional theory (DFT) solutions were used. The van der Waals dispersion corrections D3BJ³⁶ were also applied, reported to have a positive effect for telluride systems.^{37,38} The applied first-principles molecular dynamics (FPMD) technique was similar to that reported previously.^{39,40} The initial atomic configurations for glassy $\text{Ga}_{0.20}\text{Te}_{0.80}$ were created and optimized using the RMC_POT++ code⁴¹ against the experimental X-ray structure factor $S_x(Q)$ to obtain good agreement. The size of the cubic simulation box at room temperature, containing 200 atoms (40 Ga and 160 Te), was chosen to match the experimental number density. Further optimization was carried out using DFT at 0 K, applying the molecularly optimized correlation consistent with the polarized triple-zeta valence basis set along with the norm-conserving relativistic Goedecker–Teter–Hutter-type pseudopotentials.⁴² FPMD simulations were performed first at 300 K using a canonical NVT ensemble with a Nosé–Hoover^{43,44} thermostat. The simulation boxes were then heated up to 1200 K using 100 or 200 K steps for 10–15 ps each. At highest temperatures, the systems were equilibrated for 46 ps (1100 K) and 21 ps (1200 K) and cooled down to 300 K using the same temperature steps but with a longer simulation time (≈ 30 ps). Final equilibration and data collection at 300 K were performed for 73 ps. The connectivity and ring statistics were analyzed using the R.I.N.G.S.⁴⁵ and modified connectivity⁴⁶ programs. The pyMolDyn⁴⁷ code applying the Dirichlet–Voronoi principle was used for the calculation of microscopic voids.

RESULTS AND DISCUSSION

Glass-Forming Range and Thermal and Electronic Properties. Bulk $\text{Ga}_x\text{Te}_{1-x}$ alloys, $0.17 \leq x \leq 0.25$, prepared by classical melt quenching, appear to be glassy and amorphous according to laboratory X-ray diffraction; however, high-intensity synchrotron radiation yielded weak signs of crystallites in the $x = 0.25$ samples. Figure 1 shows a 2D diffraction pattern for $\text{Ga}_{0.25}\text{Te}_{0.75}$, revealing tiny diffraction

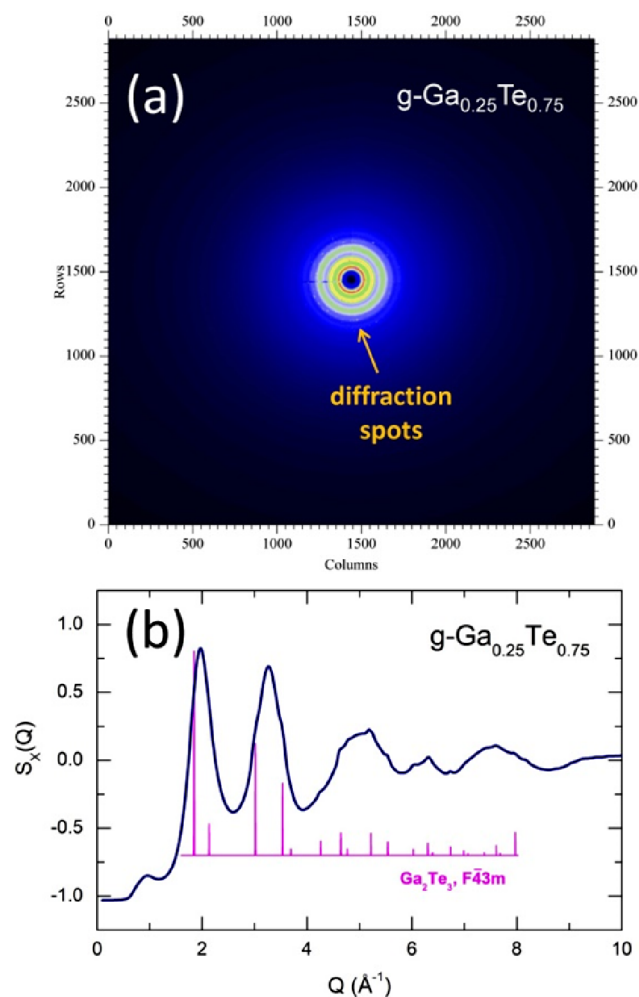


Figure 1. (a) Typical 2D image of bulk glassy Ga_{0.25}Te_{0.75} revealing tiny diffraction spots of a few nanocrystallites and (b) resulting X-ray structure factor $S_x(Q)$, which exhibits weak Bragg peaks of cubic Ga₂Te₃.⁴⁸ The most intense (111) reflection of Ga₂Te₃ at 1.84 Å⁻¹ is not visible.

spots of a few nanocrystals. The radial averaging and corresponding corrections, giving the X-ray structure factor $S_x(Q)$, exhibit weak Bragg peaks related to cubic Ga₂Te₃, space group $F\bar{4}3m$.⁴⁸ It is interesting to note that the most intense (111) crystalline reflection at 1.84 Å⁻¹ is not visible. The Te-rich samples, $x < 0.25$, were found to be completely vitreous. An MM was also used trying to expand the glass-forming range. Nevertheless, both MM-Ga_{0.15}Te_{0.85} and MM-Ga_{0.30}Te_{0.70}, prepared beyond the $0.17 \leq x \leq 0.25$ composition range, show rather intense Bragg peaks of trigonal tellurium⁴⁹ and tetragonal Ga₂Te₅^{50,51} (Figure S1). Digallium pentatelluride is a peritectic compound stable between 673 and 768 K, although a single crystal of Ga₂Te₅ was reported to be intact at room temperature for over 6 months.⁵⁰ As expected, the main crystalline phases in the MM samples were found to be consistent with the chemical composition: trigonal tellurium in MM-Ga_{0.15}Te_{0.85} and tetragonal Ga₂Te₅ ($x = 0.2857$) for MM-Ga_{0.30}Te_{0.70}.

Typical DSC traces of bulk glassy g-Ga_xTe_{1-x} are shown in Figure 2. All of the samples reveal the glass transition temperatures T_g followed by exothermic crystallization peaks, similar to those reported previously.^{13,14,52} The T_g value increases almost linearly with x from 396 to 448 K, suggesting

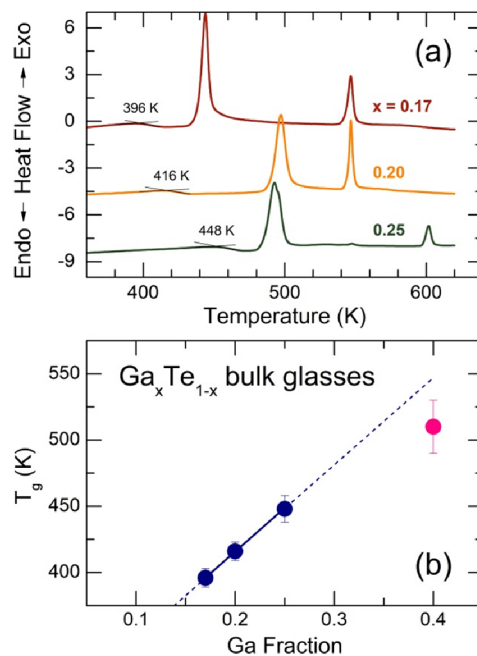


Figure 2. (a) Typical DSC traces of bulk vitreous Ga_xTe_{1-x} alloys, which exhibit glass transition temperatures T_g and exothermic crystallization features, and (b) T_g 's as a function of x ; preliminary results for the Ga₂Te₃ thin film, prepared using pulsed laser deposition, are also shown.

a high glass transition for g-Ga₂Te₃, ≈ 550 K, roughly consistent with preliminary DSC results on a Ga₂Te₃ thin film, prepared by pulsed laser deposition. The first exothermic effect was found to be related to primary tellurium crystallization, while the second exothermic feature peaked at ≈ 547 K was attributed to the remaining glass matrix crystallization of either cubic Ga₂Te₃ or tetragonal Ga₂Te₅.^{13,14,52} The 547 K feature appears to be very weak for glassy Ga_{0.25}Te_{0.75}. Instead, a distinct third exothermic effect was observed at ≈ 602 K, also reported previously for the same glass composition.¹³

To clarify the nature of crystallizing phases in glassy Ga_{0.25}Te_{0.75}, an in situ X-ray diffraction experiment has been carried out. The heating rate of the experiment has matched the DSC measurements (10 K min⁻¹), and the diffraction patterns were taken every 10 K. The sample remained glassy between room temperature and 473 K (Figure 3a). Starting from 483 K, multiple Bragg peaks have appeared, clearly visible between $1.7 \leq Q \leq 2.2$ Å⁻¹, as well as at higher scattering vectors Q . The starting temperature corresponds to the onset of primary tellurium crystallization^{13,14,52} (Figure 2a); however, the crystallizing phases were found to be more complicated (Figure 3c). In addition to expected trigonal tellurium,⁴⁹ distinct Bragg peaks of monoclinic high-pressure phase HP-Te II, space group $P2_1$ stable between 4 and 7 GPa,^{53,54} were observed as well as nonidentified reflections. Glass matrix crystallization starts above $T \geq 573$ K, and clearly visible changes appear from 593 K in agreement with the high- T exothermic peak at DSC traces. In this case also, not only usual cubic Ga₂Te₃⁴⁸ but also the rhombohedral high-pressure form HP-Ga₂Te₃, space group $R\bar{3}m$ stable above 5 GPa, was observed.⁵⁵ The population of the two polymorphs grows monotonically upon increasing T up to the maximum temperature of 643 K. We also note some nonidentified

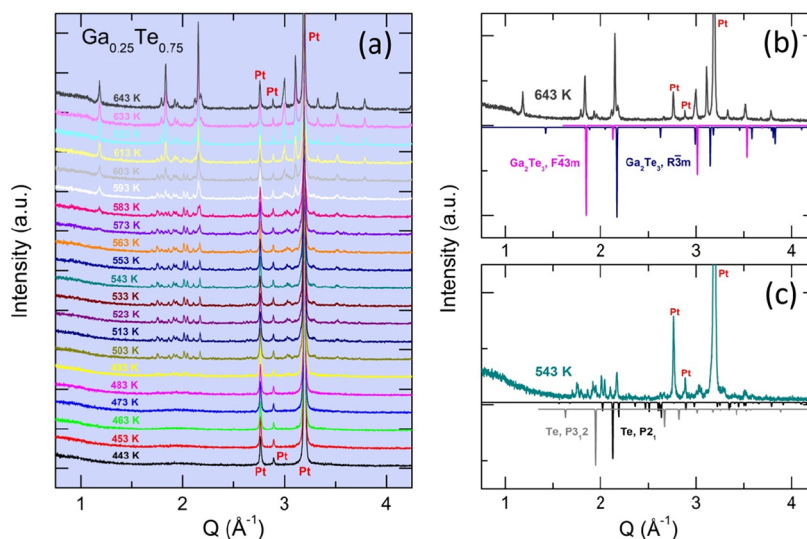


Figure 3. In situ X-ray diffraction measurements of glassy $\text{Ga}_{0.25}\text{Te}_{0.75}$ as a function of temperature: (a) diffraction patterns between 443 and 643 K (step 10 K); identification of crystallizing phases at (b) 643 and (c) 543 K. The Bragg peaks of the platinum sample holder are indicated. A distinct shift in the Bragg peak positions for rhombohedral Ga_2Te_3 is related to the difference in temperature and pressure between our measurements (643 K and ambient pressure) and high-pressure reference⁵⁵ (room temperature and 5.5 GPa).

peaks, that is, a feature at 1.185 \AA^{-1} . The high-pressure Ga_2Te_3 polymorph appears to be frozen after cooling to room temperature (Figure S2).

The observed very unusual phenomenon indicates a complex nature of Ga–Te glass crystallization involving a nanotectonic compression^{56–58} with the high internal pressure up to 4–8 GPa inside the transforming network, possibly related to a significant difference in thermal expansion coefficients between viscous metastable liquid above T_g and below T_m , and crystal phases. The observed nanocrystallites of cubic Ga_2Te_3 in glassy $\text{Ga}_{0.25}\text{Te}_{0.75}$ (Figure 1) are also reminiscent of this interfacial compression, in particular, the absence of the most intense (111) reflection at 1.84 \AA^{-1} . High-pressure X-ray diffraction studies of cubic Ga_2Te_3 have shown a monotonic decrease in strong odd-order reflections in the zinc-blende sublattice: (111) and (311), which disappear completely at 8.7 GPa.⁵⁵ The above pressure is the upper limit of a large two-phase region ($5.0 \leq P \leq 8.7$ GPa), where cubic and rhombohedral Ga_2Te_3 polymorphs coexist. Further discussions of the nanotectonic effect in glassy $\text{Ga}_x\text{Te}_{1-x}$ alloys will be made in relation with their phase-change properties.

Bulk Ga–Te glasses were reported to be narrow-gap semiconductors.^{15–17} Our conductivity and optical absorption measurements are coherent with these observations. Figure 4 shows the conductivity temperature dependence $\sigma(T)$ for bulk glassy $\text{Ga}_x\text{Te}_{1-x}$ ($x = 0.20, 0.25$) in comparison with amorphous and liquid Ga_2Te_3 ^{17,59} and liquid L- $\text{Ga}_{0.20}\text{Te}_{0.80}$.^{59–63} Previously reported data for Ga–Te glasses^{15,16} are consistent with our measurements. The glass conductivity follows the Arrhenius behavior

$$\sigma = \sigma_0 \exp(-E_a/kT) \quad (1)$$

where E_a is the activation energy and σ_0 is the pre-exponential factor. We note a significantly lower conductivity for amorphous a- Ga_2Te_3 vs g- $\text{Ga}_{0.2}\text{Te}_{0.8}$, ≈ 4 orders of magnitude at room temperature with the corresponding difference in E_a : 0.37 eV (g- $\text{Ga}_{0.2}\text{Te}_{0.8}$) and 0.56 eV (a- Ga_2Te_3) (inset in Figure 4). A similar difference was found in semiconducting liquid alloys $\text{Ga}_x\text{Te}_{1-x}$, just before a semiconductor–metal transition

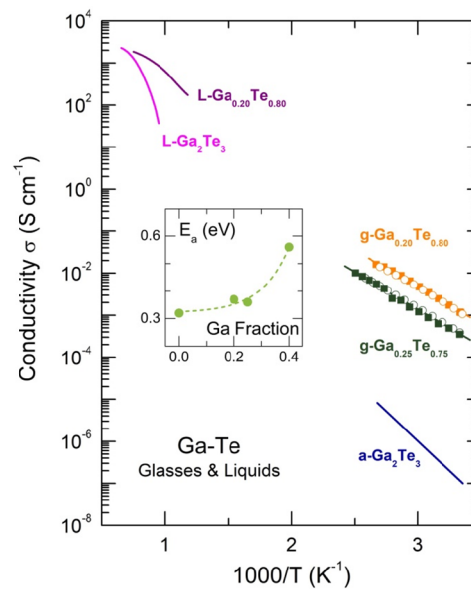


Figure 4. Conductivity temperature dependence of bulk glassy $\text{Ga}_x\text{Te}_{1-x}$, $x = 0.20, 0.25$ (this work) in comparison with amorphous and liquid Ga_2Te_3 ^{17,59} and liquid L- $\text{Ga}_{0.20}\text{Te}_{0.80}$.^{59–63} Glassy $\text{Ga}_x\text{Te}_{1-x}$: filled squares (heating) and open circles (cooling); the inset: activation energy as a function of x ; the a-Te data⁶² correspond to band-to-band conduction.

at higher temperatures $T \geq T_{\text{SCM}}$ ($x = 0.2$, $T_{\text{SCM}} = 1100$ K, and $x = 0.4$, $T_{\text{SCM}} \approx 1300$ K) with a pronounced minimum in conductivity for Ga_2Te_3 .^{59,63} This trend is partly visible in Figure 4. We also note that the conductivity pre-exponential factor, $\sigma_0 \approx 10^3 \text{ S cm}^{-1}$, indicates the electronic transport over the extended states⁶⁴ in bulk glassy Ga–Te.

The optical absorbance of bulk glassy $\text{Ga}_{0.2}\text{Te}_{0.8}$ is shown in Figure 5a over a wide wavelength range, $1.7 \leq \lambda \leq 25 \mu\text{m}$. The fundamental absorption range starts below $\approx 2.2 \mu\text{m}$, while at high λ , the IR transmittance of g- $\text{Ga}_{0.2}\text{Te}_{0.8}$ extends at least up to $25 \mu\text{m}$ as for a vast majority of vitreous tellurides.^{65–67} We note the presence of a weak absorption feature at $\approx 17 \mu\text{m}$,

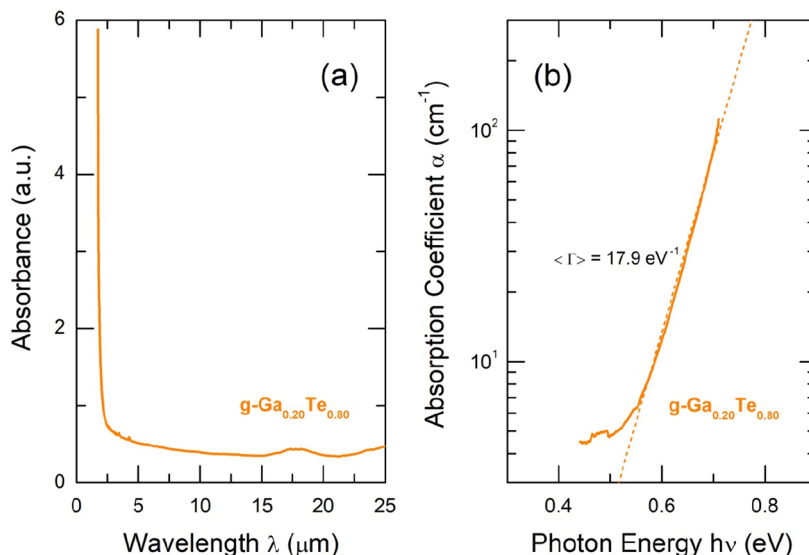


Figure 5. Optical properties of glassy $\text{Ga}_{0.2}\text{Te}_{0.8}$: (a) absorbance over a wide wavelength range up to $25 \mu\text{m}$ and (b) absorption coefficient α in the vicinity of the fundamental absorption edge.

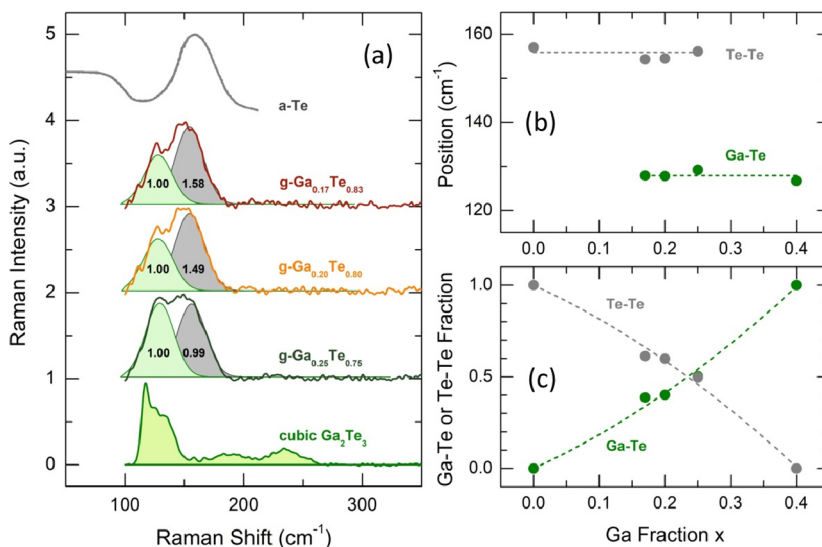


Figure 6. (a) Typical Raman spectra of bulk glassy $\text{Ga}_x\text{Te}_{1-x}$, $0.17 \leq x \leq 0.25$, amorphous tellurium,⁷² and cubic Ga_2Te_3 (this work); (b) Te–Te and Ga–Te stretching frequencies; and (c) fractional amplitudes $A_{156}(x)$ and $A_{128}(x)$ as a function of x . The dashed lines in (b) and (c) are drawn as a guide to the eye.

probably related to the second harmonics of the phonon modes and a slight increase of the absorbance above $21 \mu\text{m}$.

The absorption coefficient α was calculated taking into account the reflection corrections at the two sample/air interfaces. The reflection coefficient $R = [(n_R - 1)/(n_R + 1)]^2$, where n_R is the glass refractive index, was estimated using the Moss relation⁶⁸

$$n_R^4 E_g = 95 \text{ eV} \quad (2)$$

where E_g is the optical energy gap.

In a first approximation, the energy gap of glassy $\text{Ga}_{0.2}\text{Te}_{0.8}$ can be estimated as a weighted average of the two end members, amorphous tellurium, $E_g = 0.67 \text{ eV}$,⁶⁹ and amorphous Ga_2Te_3 , 1.09 eV .⁷⁰ The estimated optical gap for glassy $\text{Ga}_{0.2}\text{Te}_{0.8}$ appears to be 0.88 eV and the refractive index $n_R = 3.22$.

The derived absorption coefficient α is shown in Figure 5b plotted as a function of the photon energy $h\nu$. As expected for the measured range $3 \leq \alpha(h\nu) \leq 111 \text{ cm}^{-1}$, the absorption coefficient $\alpha(h\nu)$ follows a roughly exponential growth above 6 cm^{-1} with increasing photon energy (Urbach's rule)⁶⁴

$$\alpha(h\nu) = \alpha_0 \exp(\Gamma h\nu) \quad (3)$$

where α_0 is a constant and Γ is the Urbach slope. The derived average slope $\langle \Gamma \rangle = 18 \pm 1 \text{ eV}^{-1}$ is typical for chalcogenide glasses, $15\text{--}22 \text{ eV}^{-1}$.⁶⁴ The Urbach tail does not allow the optical gap to be calculated in contrast to the Tauc relation,⁷¹ observed at higher values of $\alpha > 10^4 \text{ cm}^{-1}$

$$\alpha h\nu \propto (h\nu - E_g)^k \quad (4)$$

where $k = 2$ for most chalcogenide glasses. Nevertheless, it was found that in the Urbach regime, the optical gap corresponds approximately to the photon energy at $10^2 \leq \alpha \leq 10^3 \text{ cm}^{-1}$.

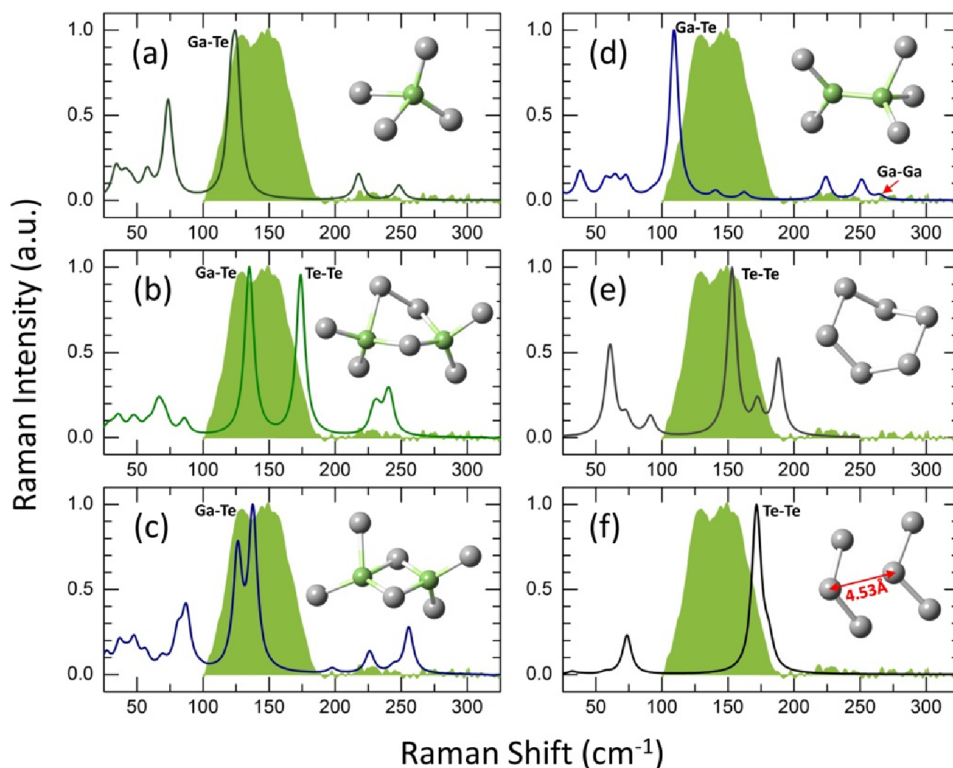


Figure 7. DFT modeling of vibrational spectra of optimized size-limited clusters: (a) isolated GaTe_4H_4 tetrahedron, (b) corner-sharing (CS)- $\text{Ga}_2\text{Te}_7\text{H}_6$ dimer, (c) edge-sharing (ES)- $\text{Ga}_2\text{Te}_6\text{H}_4$ dimer, (d) ethane-like (ETH)- $\text{Ga}_2\text{Te}_5\text{H}_5$ unit, (e) Te_6 ring, and (f) weakly interacting fragment consisting of two triatomic Te_3 oligomers, separated by 4.53 Å.³¹ The terminal hydrogen species are omitted, and the H-related vibrations are removed from the DFT spectra. The experimental Raman spectra of bulk glassy $\text{Ga}_{0.25}\text{Te}_{0.75}$ are highlighted in green in all panels.

Consequently, our estimation of the energy gap for glassy $\text{Ga}_{0.2}\text{Te}_{0.8}$ is $0.72 \text{ eV} \leq E_g \leq 0.84 \text{ eV}$, that is, reasonably consistent with the initial approximation of 0.88 eV. The derived optical gap for g- $\text{Ga}_{0.2}\text{Te}_{0.8}$ is related to the conductivity activation energy, $E_a \approx 1/2E_g$, confirming a band-to-band characteristic of the electronic transport following the electron or hole excitation above the mobility edges in the conduction or the valence bands.⁶⁴

Raman Spectroscopy and DFT Modeling. The raw Raman data for bulk Ga–Te glasses are shown in Figure S3 taking $\text{Ga}_{0.25}\text{Te}_{0.75}$ as an example. The baseline subtraction and a two-peak Gaussian fitting are also revealed. Typical normalized Raman spectra of bulk glassy Ga–Te are displayed in Figure 6 together with references: amorphous tellurium, a-Te,⁷² and cubic Ga_2Te_3 (this work). The glasses reveal a broad asymmetric poorly resolved bimodal feature centered at ≈ 128 and $\approx 156 \text{ cm}^{-1}$. The 156 cm^{-1} mode is similar to that in a-Te and Te–Te stretching modes in glassy binary tellurides: Ge–Te, As–Te, and Se–Te.^{31,73,74} The fractional amplitude of this mode $A_{156}(x)$ decreases with x , approaching zero at $x = 0.4$, $\lim_{x \rightarrow 0.4} A_{156}(x) = 0$ (Figure 6c). In contrast, the position of a lower-frequency counterpart at $\approx 128 \text{ cm}^{-1}$ is similar to that in cubic Ga_2Te_3 , and the fractional amplitude $A_{128}(x)$ increases with x and $\lim_{x \rightarrow 0.4} A_{128}(x) = 1$. Consequently, we suggest that the 128 cm^{-1} mode is related to Ga–Te stretching, while the 156 cm^{-1} feature corresponds to Te–Te vibrations.

DFT modeling of size-limiting Ga–Te clusters is consistent with the above suggestion. Isolated GaTe_4H_4 tetrahedron, corner-sharing (CS)- $\text{Ga}_2\text{Te}_7\text{H}_6$, and edge-sharing (ES)- $\text{Ga}_2\text{Te}_6\text{H}_4$ dimers exhibit the A_1 symmetric Ga–Te breathing (GaTe_4H_4) or A_1 symmetric in-phase Ga–Te breathing of CS-

or ES- GaTe_4 tetrahedra within the $124\text{--}135 \text{ cm}^{-1}$ range (Figure 7a–c). We also note that the enhanced flexibility of the CS dimer has led to the formation of a Te–Te pair and correspondingly to the Te–Te stretching at 174 cm^{-1} .

The DFT modeling of the ethane-like (ETH)- $\text{Ga}_2\text{Te}_6\text{H}_6$ cluster has shown apparent instability of this unit at 0 K. Either the ETH cluster has broken up into two GaTe_3H_3 pyramids of approximate D_{3h} symmetry, separated by 7.12 Å, or one of the tellurium species has moved from one gallium toward the other one, also forming a Te–Te pair (Figure S4). On the contrary, an ETH- $\text{Ga}_2\text{Te}_5\text{H}_5$ cluster, combining tetrahedral and trigonal gallium, appears to be stable, yielding the A_1 symmetric in-phase Ga–Te breathing mode at 109 cm^{-1} and a weak Ga–Ga stretching at 266 cm^{-1} (Figure 7d). The geometrical parameters of DFT-optimized Ga–Te clusters are collected in Table S1 and are consistent with the crystal data of the Ga–Te references.

Previous DFT modeling of $\text{Se}_x\text{Te}_{1-x}$ glasses,³¹ consisting of Se–Te chains, has shown that isolated oligomeric Se–Se, Se–Te, or Te–Te chain fragments yield blue-shifted X–X stretching vibrations, where X = Se and/or Te, because of weak interchain and strong intrachain interactions. The blue shift decreases with the increasing chain length and stronger interchain interactions. A typical example is shown in Figure 7f, where two DFT-optimized weakly interacting Te_3 triatomic oligomers reveal the A_1 in-phase Te–Te stretching at 172 cm^{-1} instead of 180 cm^{-1} for isolated triatomic units. Nevertheless, the interchain interaction was not strong enough to approach the experimental value of 157 cm^{-1} in amorphous tellurium.⁷² Surprisingly, the intraring Te–Te interactions in Te_6 or Te_8 rings correspond better to intrachain correlations in real

tellurium samples; the A_1 symmetric Te–Te stretching frequencies in tellurium rings become very close to those in a-Te and glassy binary tellurides (Figure 7e). We do not assume that Ga–Te binary glasses contain a significant population of Te_n rings but only suggest that isolated ring conformations represent better interacting oligomeric chain conformations in real glasses. The geometry of DFT-optimized tellurium rings is also given in Table S2 in good agreement with $(AgI)_2(Te_6)$ compounds and coordination polymers, consisting of Te_6 and Te_8 rings.^{75–77}

High-Energy X-ray Diffraction and First-Principles Simulations. Typical Faber–Ziman X-ray structure factors $S_X(Q)$ and interference functions $Q[S_X(Q) - 1]$ of bulk glassy binaries Ga_xTe_{1-x} are shown in Figure 8

$$S_X(Q) = w_{GaGa}(Q)S_{GaGa}(Q) + w_{GaTe}(Q)S_{GaTe}(Q) + w_{TeTe}(Q)S_{TeTe}(Q) \quad (5)$$

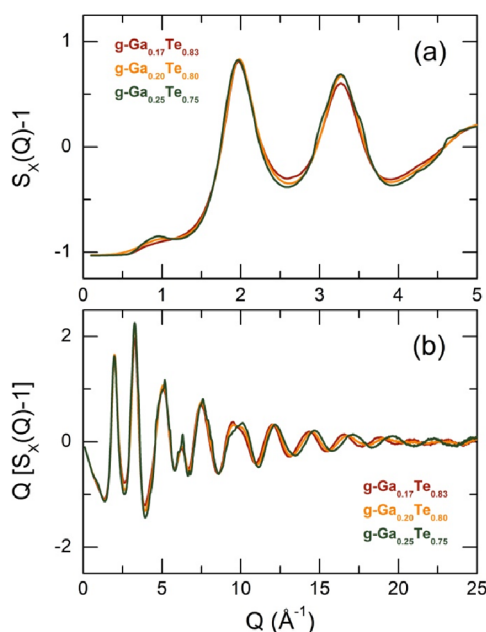


Figure 8. High-energy X-ray (a) structure factors $S_X(Q)$ over a limited Q range and (b) interference functions $Q[S_X(Q) - 1]$ of bulk glassy Ga_xTe_{1-x} , $0.17 \leq x \leq 0.25$. Ga-rich $Ga_{0.25}Te_{0.75}$ exhibits weak Bragg peaks of cubic Ga_2Te_3 ; also see Figure 1 for more details.

where $w_{ij}(Q)$ are the Q -dependent X-ray weighting coefficients and $S_{ij}(Q)$ are the Faber–Ziman partial structure factors. The two Q -space functions exhibit systematic changes. The first sharp diffraction peak (FSDP) at $Q_0 = 0.94 \pm 0.01 \text{ \AA}^{-1}$ monotonically increases with x from a nearly invisible feature for $Ga_{0.17}Te_{0.83}$ to a well-defined peak at $x = 0.25$. On the contrary, the principle peak (PP) at $Q_1 = 1.97 \pm 0.01 \text{ \AA}^{-1}$ remains essentially intact, while the amplitude of the second PP at $Q_2 \approx 3.27 \text{ \AA}^{-1}$ also increases with the gallium content. High- Q oscillations, $Q > 10 \text{ \AA}^{-1}$, are shifted to larger values with increasing x , indicating a decrease in the average interatomic distances. As mentioned above, the Ga-rich alloy, $Ga_{0.25}Te_{0.75}$, exhibits weak Bragg peaks of cubic Ga_2Te_3 ; however, the fraction of nanocrystallites appears to be insignificant. The obtained structure factors appear to be rather similar to those in bulk Ge_xTe_{1-x} binaries^{78–82} and

$Ga_xGe_xTe_{1-x}$ ternaries,^{83,84} suggesting tetrahedral gallium coordination.

The X-ray total correlation functions $T_X(r)$ obtained through the usual Fourier transform using the Lorch modification function $M(Q)$ ⁸⁵ are visualized in Figure 9

$$T_X(r) = 4\pi\rho_0 r + \frac{2}{\pi} \int_0^{Q_{\max}} Q[S_X(Q) - 1] \sin Qr M(Q) dQ \quad (6)$$

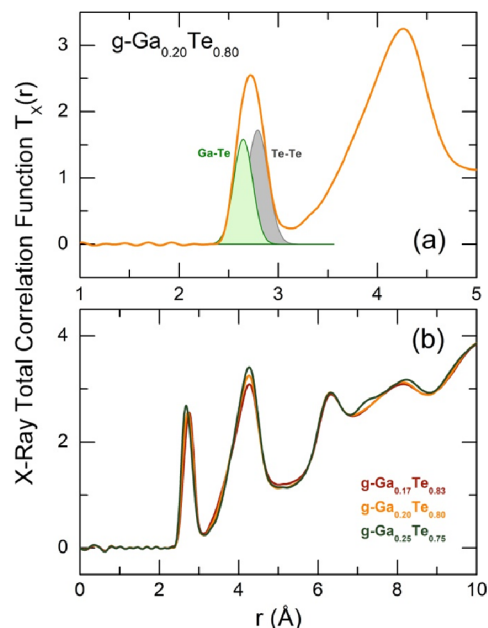


Figure 9. X-ray total correlation functions $T_X(r)$ of bulk Ga_xTe_{1-x} glasses: (a) fitting the first neighbor peak of $g-Ga_{0.20}Te_{0.80}$; the Ga–Te correlations are highlighted in light green and the Te–Te ones in light gray, and (b) $T_X(r)$ compositional trends for glassy Ga_xTe_{1-x} .

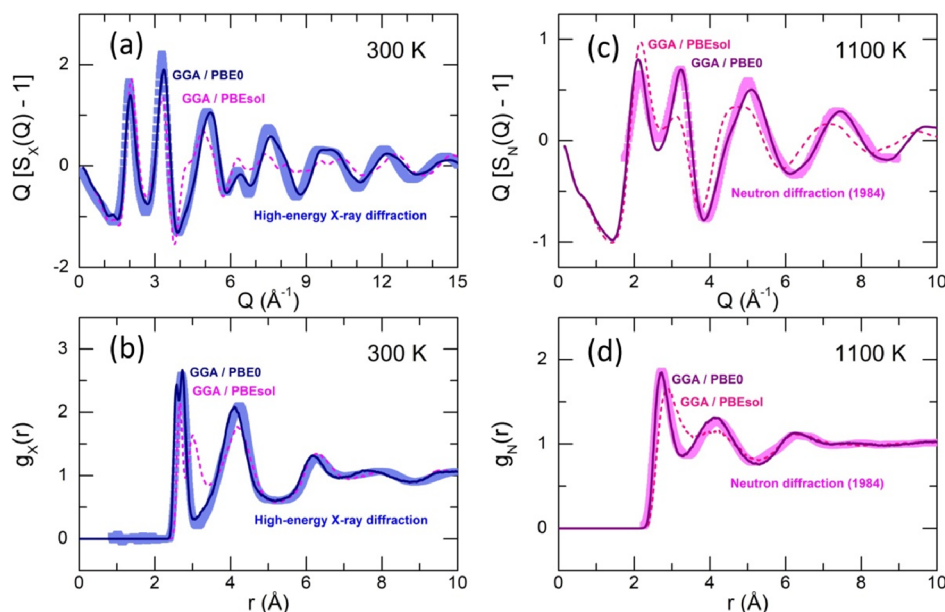
where ρ_0 is the experimental number density and $Q_{\max} = 25 \text{ \AA}^{-1}$. The asymmetric peak monotonically shifting with x from 2.75 \AA ($x = 0.17$) to 2.67 \AA ($x = 0.25$) corresponds to overlapping Ga–Te and Te–Te NN correlations. The NN peak asymmetry changes with x ; a lower r component increases simultaneously with a decreasing higher r counterpart. The unresolved asymmetric second neighbor feature is centered at 4.27 \AA and monotonically grows with x . We also note a slight trend in reducing the overlap between the NN and second neighbors. More distant correlations are less evolved except the appearance of a new shoulder at 7.2 \AA for $g-Ga_{0.25}Te_{0.75}$.

A two-peak Gaussian fitting of the NN feature unveils two contributions at 2.65 ± 0.01 and $2.80 \pm 0.01 \text{ \AA}$ (Figures 9a and S5). The 2.65 \AA peak is related to Ga–Te NN correlations and consistent with the Ga–Te interatomic distances in crystalline tellurides, 2.55 – 2.67 \AA ,^{48,50,86} and $Ga_xGe_xTe_{1-2x}$ ternary glasses, 2.63 – 2.64 \AA .^{83,84} The 2.80 \AA feature corresponds to Te–Te NN contacts and also appears to be in good agreement with crystalline and amorphous references: trigonal tellurium: 2.835 \AA ,⁴⁹ amorphous Te: 2.80 \AA ,⁸⁷ and $Ga_xGe_xTe_{1-2x}$ ternary glasses: 2.74 – 2.83 \AA .^{83,84} The constrained fitting suggesting a tetrahedral gallium local environment, $N_{Ga-Te} \cong 4$, yields the average tellurium coordination, $2.20 \leq N_{Te-X} = N_{Te-Ga} + N_{Te-Te} \leq 2.43$ (Table 1), and a reasonable approximately two-fold coordination for tellurium

Table 1. Nearest-Neighbor Interatomic Distances r_{ij} and Partial Coordination Numbers N_{ij} in Experimental and FPMD Data for Bulk Glassy $\text{Ga}_x\text{Te}_{1-x}$

x	Ga–Ga		Ga–Te		Te–Te		$N_{\text{Ga}-x}$	$N_{\text{Te}-x}$
	$r_{\text{Ga-Ga}}$ (Å)	$N_{\text{Ga-Ga}}$	$r_{\text{Ga-Te}}$ (Å)	$N_{\text{Ga-Te}}$	$r_{\text{Te-Te}}$ (Å)	$N_{\text{Te-Te}}$		
Experimental X-ray Data								
0.17			2.66(1)	4.00	2.80(1)	1.38(4)	4.00	2.20(8)
0.20			2.65(1)	3.96	2.79(1)	1.30(5)	3.96	2.29(10)
0.25			2.64(1)	3.99	2.80(1)	1.10(5)	3.99	2.43(10)
FPMD Data								
0.20			2.59(2)	3.99(2)	2.78(2)	1.33(4)	3.99(2)	2.33(5)
0.20 ^a			2.62(2)	4.02(2)	2.83(2)	1.53(5)	4.02(2)	2.54(6)
0.20 ^b	2.46(1)	0.09(2)	2.64(2)	3.93(4)	2.84(3)	1.54(5)	4.02(5)	2.52(6)

^aSupercooled liquid at 600 K. ^bMetallic liquid at 1100 K.

**Figure 10.** Experimental and FPMD simulated interference functions (a) $Q[S_X(Q) - 1]$ (this work), (c) $Q[S_N(Q) - 1]$ ¹⁹ and pair-distribution functions, (b) $g_X(r)$ (this work), and (d) $g_N(r)$ ¹⁹ for $\text{Ga}_{0.2}\text{Te}_{0.8}$. The solid lines represent the FPMD results with hybrid functionals, GGA/PBE0, and the dashed lines with classical GGA/PBEsol.

species, not involved in the Te–Ga bonding. The partial Te–Te coordination number for these species $N_{\text{Te-Te}}^* = N_{\text{Te-Te}}(1-x)/(1-2.5x)$ slightly increases with x from $N_{\text{Te-Te}}^* = 1.99 \pm 0.05$ ($x = 0.17$) to 2.20 ± 0.10 ($x = 0.25$).

The FPMD modeling of $\text{Ga}_{0.2}\text{Te}_{0.8}$ was focused on atomic structures at 300, 600, and 1100 K undergoing the following changes: (i) solid glass–viscous supercooled liquid and (ii) semiconducting liquid–metallic melt. The neutron diffraction data for metallic $\text{Ga}_{0.2}\text{Te}_{0.8}$ were available only in a limited Q range from 1.7 to 9 \AA^{-1} and represent a linear interpolation between $\text{Ga}_{0.14}\text{Te}_{0.86}$ and $\text{Ga}_{0.28}\text{Te}_{0.72}$ melts.¹⁹ As previously reported,^{74,88,89} the used hybrid GGA/PBE0 functional has a clear advantage compared to GGA/PBE or GGA/PBEsol both for glasses and liquids, except associated heavy computational costs. Figure 10 illustrates a distinct difference in the glass and liquid interference $Q[S_X(Q) - 1]$ and pair-distribution $g_X(r)$ functions in direct comparison with experimental data. As expected, the interatomic distances, especially the Te–Te separations, are overestimated for the GGA/PBEsol simulations even with van der Waals dispersion corrections.

The derived GGA/PBE0 partials in Q and r space are shown in Figure 11. The Ga–Ga partial structure factor $S_{\text{GaGa}}(Q)$

exhibits a strong FSDP at $Q_0 = 0.85 \text{ \AA}^{-1}$ (300 K) and 0.82 \AA^{-1} (1100 K). Nevertheless, this contribution is weak in the total X-ray structure factor (Figure 8a) because of the negligible weighting coefficient, $\langle w_{\text{GaGa}}^X(Q) \rangle = 0.0132 \pm 0.0003$. The angle brackets indicate the $w_{\text{GaGa}}^X(Q)$ averaging over the used Q range. The largest weighting has the $S_{\text{TeTe}}(Q)$ partial, $\langle w_{\text{TeTe}}^X(Q) \rangle = 0.7838 \pm 0.0022$. The FSDP is more visible in neutron data ($w_{\text{GaGa}}^N = 0.05714$); however, we cannot compare the simulated neutron structure factor at low Q with the experimental $S_N(Q)$, because of limited Q range of the available neutron diffraction results.¹⁹

The derived Ga–Te and Te–Te nearest-neighbor positions in r space are similar to the experimental separations as well as the partial coordination numbers (Table 1). Liquid $\text{Ga}_{0.2}\text{Te}_{0.8}$ at 1100 K shows a small fraction of Ga–Ga homopolar bonds, $N_{\text{Ga-Ga}} = 0.09 \pm 0.02$, indicating a partial dissociation, $2\text{Ga-Te} \rightleftharpoons \text{Ga-Ga} + \text{Te-Te}$. The derived Ga–Ga NN distances, $2.46 \pm 0.01 \text{ \AA}$, are consistent with the crystal data in monoclinic GaTe , $2.433 \pm 0.003 \text{ \AA}$,⁸⁶ and trigonal $\text{Ga}_7\text{Te}_{10}$, $2.475 \pm 0.002 \text{ \AA}$.⁹⁰ Gallium is four-fold-coordinated, $N_{\text{Ga-X}} = N_{\text{Ga-Te}} + N_{\text{Ga-Ga}} \cong 4.0$, in both glasses and liquids, while the

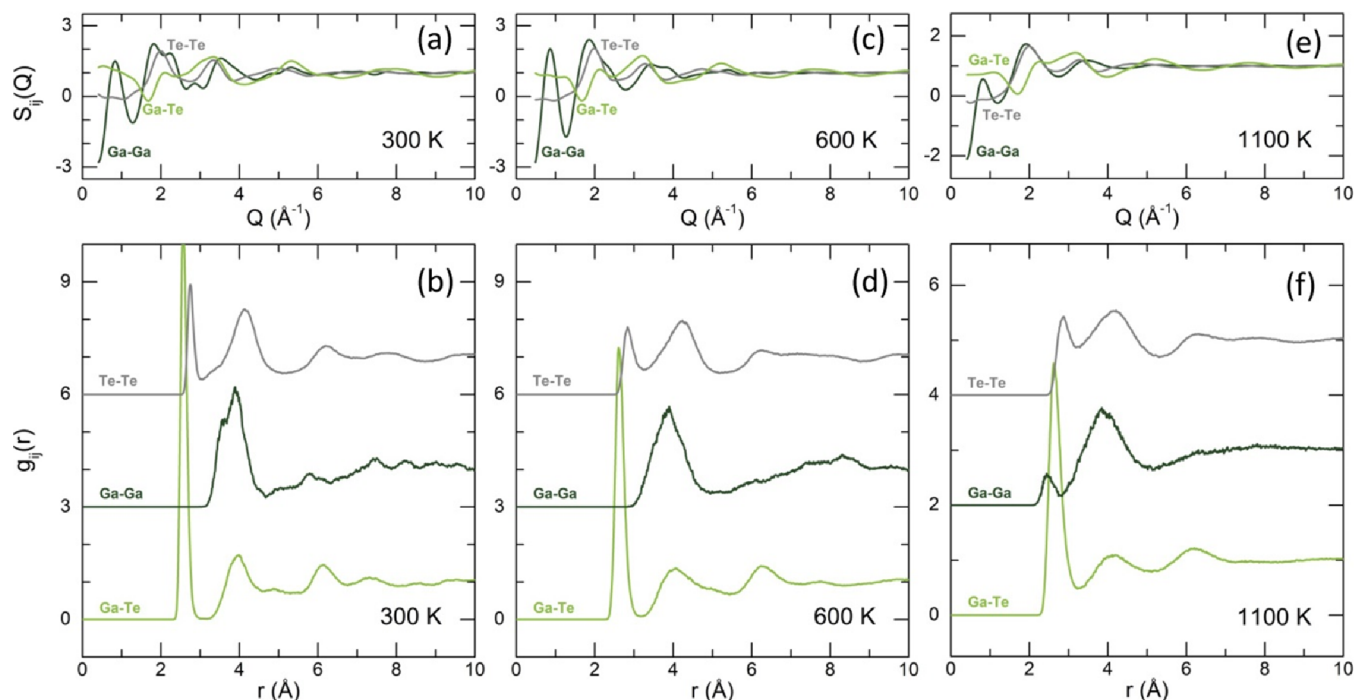


Figure 11. FPMD partial structure factors $S_{ij}(Q)$ for (a) glassy $\text{Ge}_{0.2}\text{Te}_{0.8}$ at 300 K, (c) supercooled (600 K), and (e) metallic (1100 K) liquid $\text{Ge}_{0.2}\text{Te}_{0.8}$; (b,d, and f) corresponding pair-distribution functions $g_{ij}(r)$, simulated using the GGA/PBE0 hybrid exchange-correlation functional.

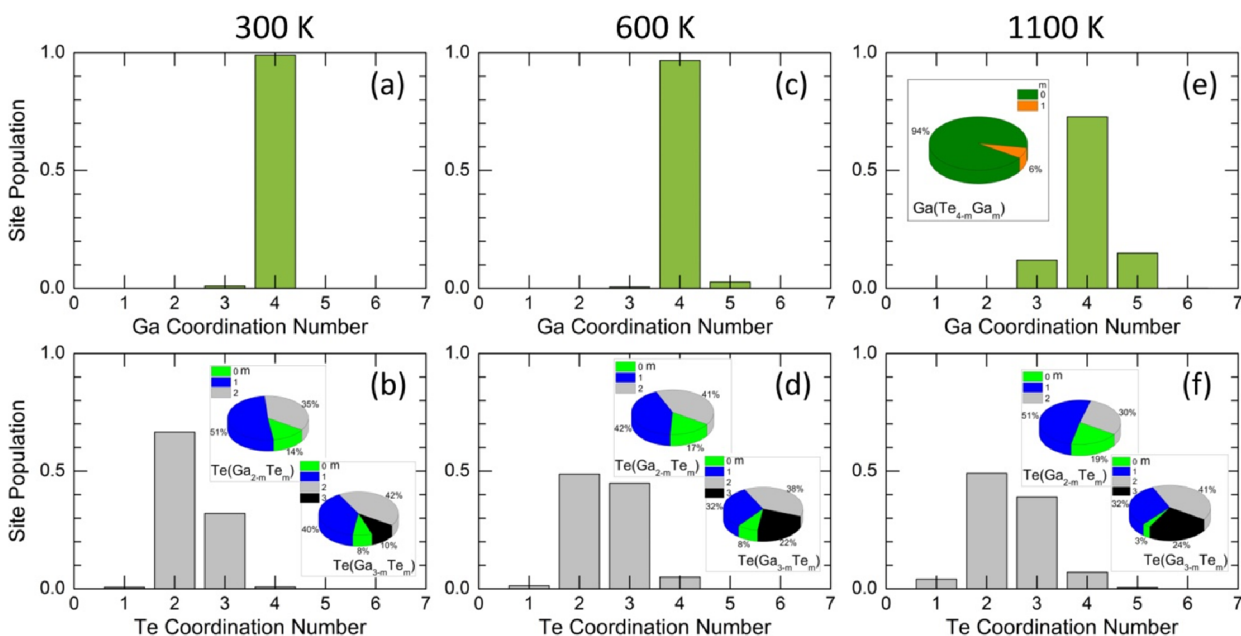


Figure 12. GGA/PBE0-derived (a,c, and e) gallium and (b,d, and f) tellurium coordination numbers in glassy (300 K), supercooled (600 K), and metallic (1100 K) liquid $\text{Ga}_{0.2}\text{Te}_{0.8}$. The insets show the NN distributions around central Ga, two-fold, and trigonal Te species. The enlarged insets are also given in Figure S6.

Te–Te partial coordination number increases with temperature, $N_{\text{Te-Te}} = 1.33 \pm 0.04$ (300 K) and 1.54 ± 0.05 (1100 K) (Table 1). In other words, the fraction of two-fold coordinated chain-like Te–Te fragments decreases from 87% in semi-conducting glass to 54% in supercooled semiconducting (600 K) or metallic (1100 K) liquid. Surprisingly, the semiconductor-to-metal transition in Ga–Te alloys was not associated with a Peierls distortion as in the case of Ge–Te and other telluride systems. The local gallium coordination

remains intact (Table 1) as well as the shape and position of the first neighbor peak for $g_{\text{GaTe}}(r)$ partials (Figure 11). In contrast, the Ge–Te NN distances in GeTe_2 become markedly longer in metallic liquid, and the $g_{\text{GeTe}}(r)$ partial function exhibits an asymmetric shape with a long- r tail without a clear minimum.⁷⁴

Gallium distribution in glassy and liquid $\text{Ga}_{0.2}\text{Te}_{0.8}$ is far from random. Only 15% of Ga species are located between ≈ 4 and 6 \AA from each other, while the average Ga–Ga interatomic

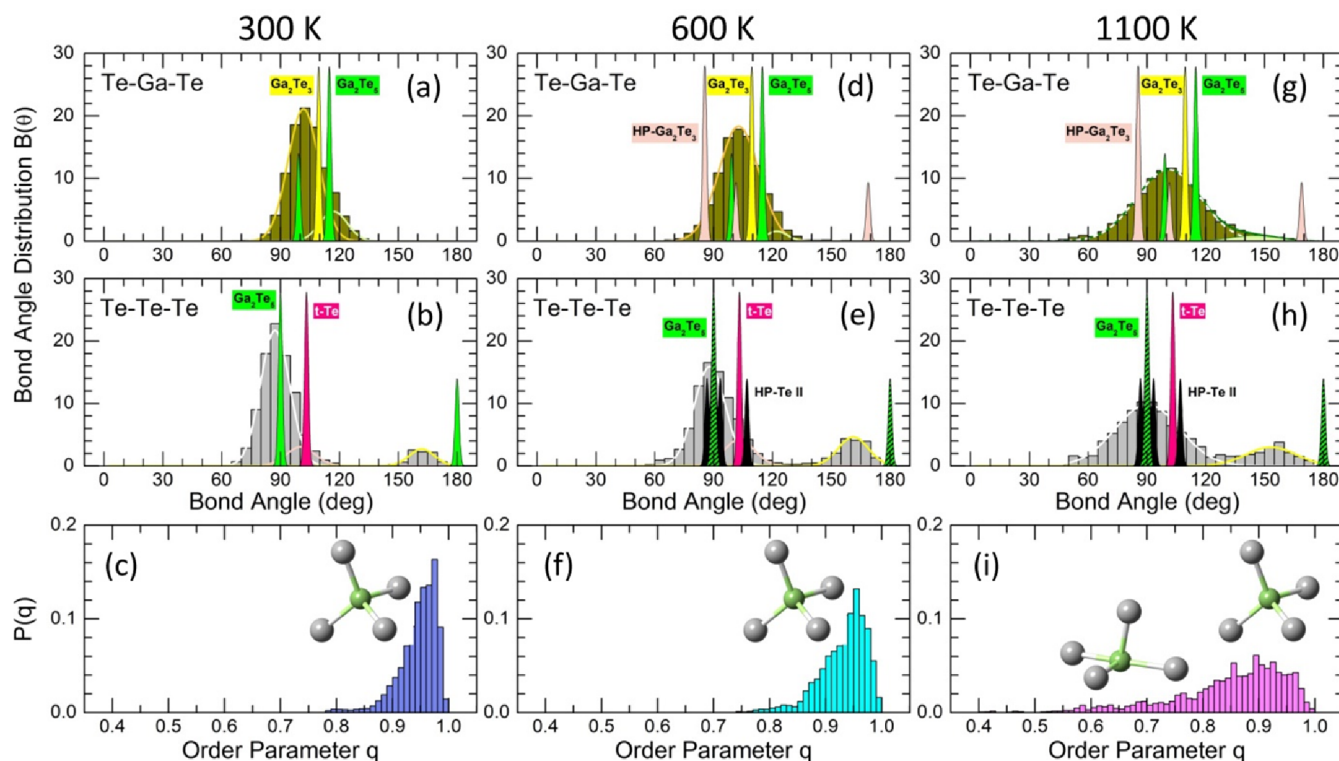


Figure 13. GGA/PBE0-derived (a,d, and g) Te–Ga–Te and (b,e, and h) Te–Te–Te bond angle distributions $B(\theta)$ in $\text{Ga}_{0.2}\text{Te}_{0.8}$ at 300, 600, and 1100 K; (c,f, and i) corresponding T -dependent orientational order parameter q .^{91,92} Bond angle positions in crystalline references: cubic Ga_2Te_3 ,⁴⁸ high-pressure rhombohedral HP- Ga_2Te_3 ,⁵⁵ tetragonal Ga_2Te_3 ,^{50,51} trigonal tellurium t-Te,⁴⁹ and high-pressure monoclinic HP-Te II,⁵³ are also shown in the respective $B(\theta)$ panels.

distance is expected to be 5.6 Å, corresponding to a random distribution. The remaining 85% have at least one gallium neighbor at a distance $r_{\text{GaGa}} \lesssim 4$ Å. The majority are forming connected groups of CS and ES Ga–Te polyhedra consisting of 2–12 members. The ES species represent a clear minority: 5% at 300 K and 18% at 1100 K. Tellurium connectivity is drastically different because of the predominant Te content in $\text{Ga}_{0.2}\text{Te}_{0.8}$. Consequently, $\approx 12\%$ of Te has exclusively gallium NNs, and a vast majority forms Te_n fragments, $2 \leq n \leq n_{\text{max}} = 21\text{--}36$, depending on temperature and statistical fluctuations.

Figure 12 shows the coordination distributions for gallium and tellurium in glassy and liquid $\text{Ga}_{0.2}\text{Te}_{0.8}$. The Ga coordination is four-fold ($99 \pm 2\%$) and pure (only Te NNs) in the solid glass; the population of three-fold coordinated gallium species is negligible. Supercooled and metallic liquids exhibit both under- and over-coordinated gallium, but the fraction of four-fold coordinated species is predominant, $97 \pm 3\%$ (600 K) and $73 \pm 5\%$ (1100 K). The majority of four-fold coordinated gallium in metallic liquid, 94%, consists of GaTe_4 units; the mixed Ga environment, $\text{Ga}(\text{Te}_{4-m}\text{Ga}_m)$, is minor and exclusively contains Ga–Ga dimers, $m = 1$. The average tellurium coordination in glassy $\text{Ga}_{0.2}\text{Te}_{0.8}$, $N_{\text{Te-X}} = 2.33 \pm 0.05$, indicates that two-thirds of Te species are two-fold-coordinated (Figure 12b). The remaining tellurium is mostly trigonal; the fractions of terminal $\text{Te}_{1\text{F}}$ and four-fold coordinated tellurium $\text{Te}_{4\text{F}}$ are very small, $\approx 0.7\%$ each. The increasing Te coordination in both supercooled and metallic liquid, $N_{\text{Te-X}} \cong 2.53$, suggests comparable populations of chain-like and trigonal tellurium. In addition, the fractions of under- and over-coordinated species are also increased, in

particular, by a factor of ≈ 6 (600 K) and ≈ 10 (1100 K) for $\text{Te}_{4\text{F}}$.

The Te local environment is essentially mixed. Approximately, one-half of the chain-like species, $\text{Te}(\text{Ga}_{2-m}\text{Te}_m)$, have one Ga and one Te NN ($m = 1$) in glassy and liquid $\text{Ga}_{0.2}\text{Te}_{0.8}$ (the insets in Figures 12b,d,f and S6). The Te–Te dimers and oligomeric chain fragments Te_n ($m = 2$, $2 \leq n \leq n_{\text{max}}$) represent \approx one-third of two-fold coordinated tellurium. The remaining, Ga–Te–Ga, bridges, $m = 0$, appear to be the minority entities (14–19%). More than half of trigonal $\text{Te}(\text{Ga}_{3-m}\text{Te}_m)$ units are tellurium-rich species, $m \geq 2$. Pure heteropolar Te-centered units TeGa_3 appear to be negligible, $6 \pm 2\%$.

The geometry of Ga-centered units, reflected by the Te–Ga–Te bond angles, depends on temperature (Figure 13a,d,g). A broad asymmetric $B_{\text{TeGaTe}}(\theta)$ distribution in the solid glass deviates from the regular tetrahedral shape characteristic of cubic Ga_2Te_3 .⁴⁸ The $B_{\text{TeGaTe}}(\theta)$ is centered at 102° instead of 109.47° and has a shoulder at 117° . A similar shape has slightly distorted tetrahedra in tetragonal Ga_2Te_3 .^{50,51} The GaTe_n units, $3 \leq n \leq 5$, in the metallic liquid $\text{Ga}_{0.2}\text{Te}_{0.8}$ show a much wider $B_{\text{TeGaTe}}(\theta)$ distribution centered at 101° . In addition, we note a weak high-angle shoulder at 145° , highlighted in light green in Figure 13g. The apparent almost symmetric shape of the main feature seems to be hiding various geometries of the GaTe_n units, including distorted defect octahedra without one or two Te NNs around central Ga, whose geometry is reminiscent of the high-pressure rhombohedral HP- Ga_2Te_3 polymorph⁵⁵ (Figure S7). The tetrahedral orientational order parameter q ^{91,92} is consistent with this hypothesis

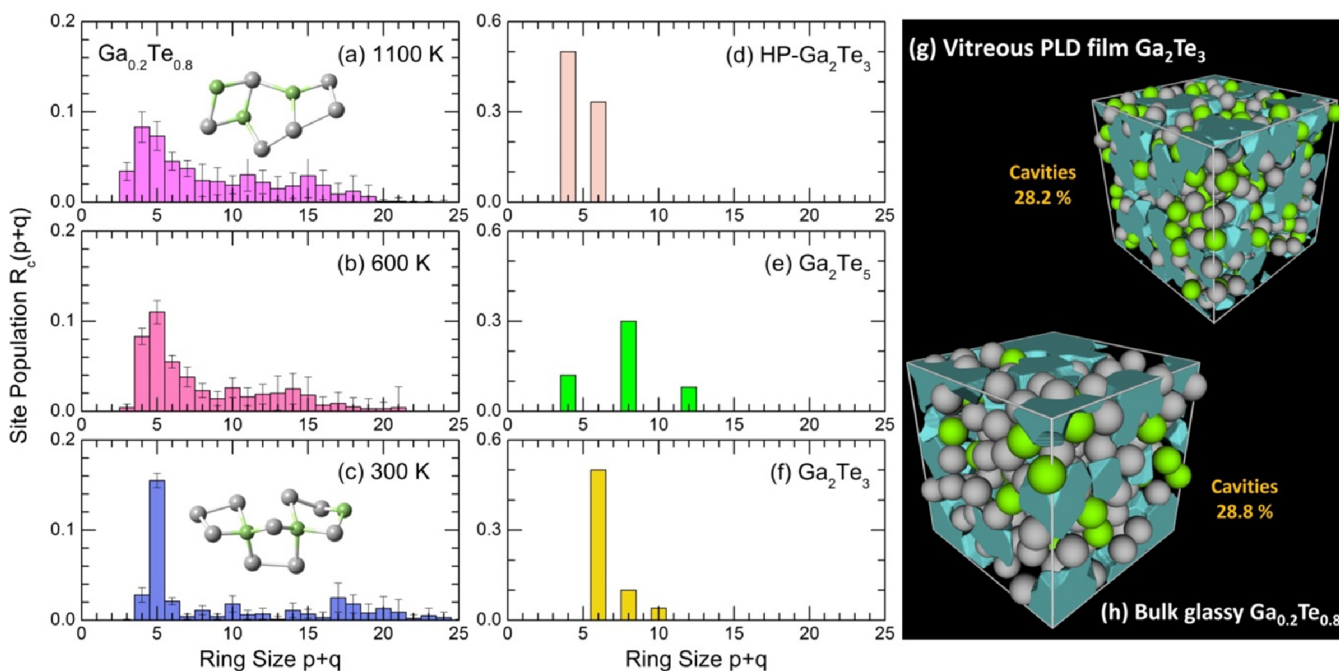


Figure 14. Ring statistics in (a) metallic (1100 K) liquids, (b) supercooled (600 K) liquids, and (c) glassy $\text{Ga}_{0.2}\text{Te}_{0.8}$, as well as in crystalline references: (d) high-pressure rhombohedral HP- Ga_2Te_3 , (e) tetragonal Ga_2Te_5 , and (f) cubic Ga_2Te_3 . The insets show typical rings in metallic liquid and solid glass. Voids and cavities in (g) vitreous PLD film Ga_2Te_3 (preliminary results) and (h) bulk glassy $\text{Ga}_{0.2}\text{Te}_{0.8}$.

$$q = 1 - \frac{3}{8} \sum_{j=1}^3 \sum_{k=j+1}^4 \left(\cos \psi_{jk} + \frac{1}{3} \right)^2 \quad (7)$$

where ψ_{jk} is the Te–Ga–Te angle of a given GaTe_4 unit. The average value of q changes between 0 for an ideal gas and $q = 1$ for a regular tetrahedral network.

The $P(q)$ probability distribution function in glassy $\text{Ga}_{0.2}\text{Te}_{0.8}$ peaks at $q = 0.97$ and appears to be consistent with a distorted tetrahedral topology of GaTe_4 units (Figure 13c). A broad asymmetric $P(q)$ function in metallic liquid is centered at $q \approx 0.9$ and exhibits a long tail up to $q = 0.4$ (Figure 13i). The low- q part, $0.4 \lesssim q \lesssim 0.8$, is typical for distorted defect octahedra.⁷⁴ A regular defect octahedron GaTe_4 , with $\theta_{\text{Oh}}(1) = \pi$ and $\theta_{\text{Oh}}(2) = \pi/2$, has $q = 5/8$, that is, just in the middle of this q range. The characteristic shapes of distorted tetrahedra ($q = 0.97$) and defect octahedra ($q = 0.6$) are also shown in Figure 13c,f,i. The fraction of nontetrahedral species ($q \lesssim 0.8$) increases with T , $1 - f_{\text{Td}}$: 2.3% (300 K), 4.6% (600 K), and 27.1% (1100 K), where f_{Td} is the tetrahedral fraction.

The geometry of GaTe_3 and GaTe_5 units is also variable (Figure S8). The three-fold gallium entities mostly adopt a pyramidal shape, while the GaTe_5 species are divided between trigonal bipyramids and defect octahedra of HP- Ga_2Te_3 type (see the Supporting Information for more details).

The excessive tellurium in $\text{Ga}_{0.2}\text{Te}_{0.8}$ does not follow the chainlike geometry of trigonal t-Te (Figure 13b,e,h). The $B_{\text{TeTeTe}}(\theta)$ distribution is essentially bimodal with the main contribution at $\approx 90^\circ$ and a minor high-angle part centered between 163° (300 K) and 153° (1100 K), instead of a predominant feature at 103° , characteristic of t-Te⁴⁹ and shown by a pink-colored peak in Figure 13b,e,h. Glassy $\text{Ga}_{0.2}\text{Te}_{0.8}$ still reveals a weak shoulder (11%) at 100° similar to t-Te, but the main tellurium connectivity is reminiscent of the

Te sublattice in tetragonal Ga_2Te_5 . It should also be noted that similar $B_{\text{TeTeTe}}(\theta)$ distribution has amorphous and liquid Te^{93–95} and high-pressure monoclinic HP-Te II,⁵³ whose 2D puckered layers are formed by distorted “square” rings (Figure S7). Consequently, we assume that two defect motifs of HP-Te II and Ga_2Te_5 seem to be the origin of the observed Te-related geometry in supercooled and metallic liquids $\text{Ga}_{0.2}\text{Te}_{0.8}$ (also see Figure S7 for visual comparison of FPMD-derived network fragments with these crystals).

The relatively small Ga fraction in $\text{Ga}_x\text{Te}_{1-x}$ binaries, $0.17 \leq x \leq 0.25$, raises a question of how the alloying with gallium changes the structure of amorphous and liquid tellurium.^{93–95} Basically, the Te-rich subnetwork of $\text{Ga}_x\text{Te}_{1-x}$ alloys exhibits similar structural features: the average Te local coordination $N_{\text{Te-Te}} > 2$, mostly consisting of chain-like and trigonal Te species, and a bimodal $B_{\text{TeTeTe}}(\theta)$ bond angle distribution peaked at $\approx 90^\circ$ with a minor high-angle part, $158^\circ \pm 5^\circ$, depending on temperature. Usually, these features suggest a defect octahedral environment for tellurium. In addition, they can also be interpreted as a signature of high-pressure motifs typical for monoclinic HP-Te II (Figure S7), consisting of four-fold rings. Ring statistics in both amorphous and liquid tellurium^{93–95} also shows a significant fraction of Te_4 rings.

The intermediate range order in liquid and glassy $\text{Ga}_{0.2}\text{Te}_{0.8}$ is given by the Ga_pTe_q ring statistics. Five-fold rings are dominating in the solid glass (Figure 14c). The population of any other ring size is substantially lower, at least by a factor of 5. The size distribution $R_c(p+q)$ ⁴⁵ is rather monotonic, except for $p+q = 5$, and extends up to 25-fold rings with an additional weak and broad maximum at $p+q = 18 \pm 2$. In the two liquids, especially at 1100 K, big rings have rather short life expectancy, shown by a large uncertainty in their population; the fraction of small long-living rings, essentially limited by seven-fold entities, rises up sharply. The network topology is quite different from crystalline references, whose ring statistics

is also given in Figure 14d–f. We also note a constant growth of “square” rings with temperature, exceeding the population of five-fold moieties in metallic liquid $\text{Ga}_{0.2}\text{Te}_{0.8}$. A rough similarity can be found comparing the lattice topology in semiconducting cubic and metallic rhombohedral gallium sesquitelluride Ga_2Te_3 .

Voids and cavities in glassy $\text{Ga}_{0.2}\text{Te}_{0.8}$, calculated using the Dirichlet–Voronoi tessellation,⁴⁷ are also shown in Figure 14 in comparison with stoichiometric vitreous PLD film Ga_2Te_3 (preliminary results). The cavity fraction V_c , normalized to the volume of the FPMD simulation box, appears to be very similar in the two cases, $28.5 \pm 0.3\%$. Te-rich binary and ternary alloys,^{83,95} including amorphous and liquid Te,^{93–95} a-Sb₂Te₃,⁹⁶ a-In₂Te₃,⁶ and g-GeTe₂,⁷⁴ reveal comparable V_c values in a marked contrast with Te-poor compositions, that is, GeTe having $V_c = 8 \pm 2\%$.^{96,97}

The electronic density of states derived from the Kohn–Sham eigenvalue spectra is shown in Figure 15 for solid glass

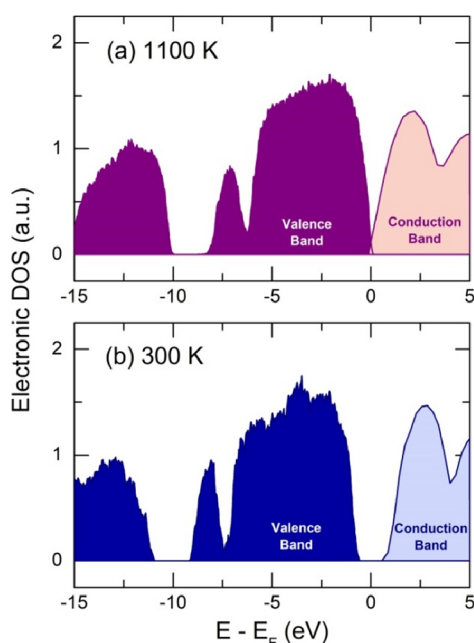


Figure 15. Electronic density of states for (a) metallic liquid at 1100 K and (b) semiconducting glass $\text{Ga}_{0.2}\text{Te}_{0.8}$ at 300 K ($E_g^{\text{PBE0}} = 1.14$ eV).

(300 K) and metallic liquid (1100 K). The calculated band gap, $E_g^{\text{PBE0}} = 1.14$ eV for glassy $\text{Ga}_{0.2}\text{Te}_{0.8}$, is slightly overestimated compared to the experimental results, $0.72 \text{ eV} \leq E_g \leq 0.84 \text{ eV}$. The PBE0 hybrid functional is known by overestimating the band gap.⁹⁸ As expected, liquid $\text{Ga}_{0.2}\text{Te}_{0.8}$ appears to be metallic.

Atomic Structure Evolution as a Function of Temperature

The average four-fold gallium coordination remains essentially intact in glassy, supercooled, and metallic liquid forms of $\text{Ga}_{0.2}\text{Te}_{0.8}$; however, the fraction of tetrahedral species, f_{T_4} , and the population of under- and over-coordinated gallium, $p_{\text{Ga}\neq 4}$, evolve substantially with an increase in temperature. The changes are rather small in the supercooled liquid at 600 K, $f_{\text{T}_4} \approx 0.95$, and $p_{\text{Ga}\neq 4} \approx 0.03$, but seem to be rising sharply on a semiconductor–metal transition above melting. Metallic $\text{Ga}_{0.2}\text{Te}_{0.8}$ at 1100 K reveals $f_{\text{T}_4} \approx 0.73$ and

$p_{\text{Ga}\neq 4} = 0.27 \pm 0.05$. In addition, homopolar Ga–Ga bonds arise in the metallic melt, $\chi = N_{\text{GaGa}}/(N_{\text{GaGa}} + N_{\text{GaTe}}) \cong 0.02$.

In contrast, the tellurium local environment transforms drastically above the glass transition and basically persists for both supercooled and metallic liquids. The average tellurium coordination increases by 9%, from $N_{\text{Te-X}} = 2.33$ (300 K) to ≈ 2.53 (600–1100 K) with comparable populations of two-fold and trigonal Te, and the fractions of terminal $\text{Te}_{1\text{F}}$ and four-fold $\text{Te}_{4\text{F}}$ species explode by a factor of 5–10.

Comparing the obtained GGA/PBE0 results for $\text{Ga}_{0.2}\text{Te}_{0.8}$ with FPMD and RMC modeling of ternary $\text{Ga}_x\text{Ge}_x\text{Te}_{1-2x}$ glasses and liquids,^{83,84,99} we note both similarities and differences. A common feature appears to be a predominant four-fold and tetrahedral gallium environment. In glassy $\text{Ga}_{0.11}\text{Ge}_{0.11}\text{Te}_{0.78}$, the population of under- and over-coordinated Ga species is $p_{\text{Ga}\neq 4} < 0.01$,⁸³ the $\text{Ga}_x\text{Ge}_x\text{Te}_{1-2x}$ liquids, $0.06 \leq x \leq 0.14$, are characterized by $p_{\text{Ga}\neq 4} = 0.20 \pm 0.02$ and $f_{\text{T}_4} = 0.75 \pm 0.05$.⁹⁹ Similar results were also reported for amorphous and liquid In_2Te_5 and In_2Te_3 ,^{6,100} while glassy and liquid $\text{Ge}_x\text{Te}_{1-x}$ binaries exhibit higher $p_{\text{Ga}\neq 4}$ and lower f_{T_4} .^{38,96,101,102} The average tellurium coordination

$N_{\text{Te-X}}$ strongly depends on the choice of the exchange-correlation functional and dispersion corrections and/or modeling procedure and method. For glassy $\text{Ga}_{0.11}\text{Ge}_{0.11}\text{Te}_{0.78}$, the Te coordination was found to be $N_{\text{Te-X}} = 2.59$ (RMC-refined GGA/PBEsol approximation),⁸³ while ND, high-energy XRD, and EXAFS experimental results fitted using large RMC simulation boxes up to 40,000 atoms reveal 2.07 ($x = 0.075$) $\leq N_{\text{Te-X}} \leq 2.35$ ($x = 0.143$).⁸⁴ A similar situation was also found for $\text{Ge}_x\text{Te}_{1-x}$ glasses.^{38,96,101,103} The average tellurium coordination increases for $\text{Ga}_x\text{Ge}_x\text{Te}_{1-2x}$ and $\text{Ge}_x\text{Te}_{1-x}$ liquids compared to glasses, but once again the classical PBE or PBEsol functionals usually yield higher $N_{\text{Te-X}}$ than hybrid BLYP or RMC.

Nanotectonic Compression and Phase-Change Properties. One of the two logic states for phase-change memory applications, the crystalline or SET state, seems to have a complicated composition and crystal structure for Te-rich binaries. The equilibrium Ga–Te phase diagram¹⁰⁴ predicts a crystallization path for $\text{Ga}_x\text{Te}_{1-x}$ glasses, $0.17 \leq x \leq 0.25$, with transformation into Ga_2Te_3 and Te, basically consistent with our XRD measurements (Figures 1, 3, and S2). However, the crystallization processes appear to be more complicated than expected. Particularly, in addition to stable cubic Ga_2Te_3 with a defective zinc blende-like structure, high-pressure rhombohedral Ga_2Te_3 was also observed (Figures 3 and S2), whose structure consists of repeated quintuple layers of atoms, Te2–Ga–Te1–Ga–Te2 stacking along the *c* axis of the unit cell.⁵⁵ In contrast to all known ambient pressure phases in the Ga–Te system, the gallium local coordination in rhombohedral Ga_2Te_3 is octahedral, and tellurium is four-fold-coordinated on average (one Te1 and two Te2 yield the average coordination $\langle N_{\text{Te-Ga}} \rangle = (6 + 3 \times 2)/3 = 4$, Figure S7).

The complicated crystallization path for Ga–Te binaries could affect the switching rate of a PCM device. Nevertheless, crystallization processes in a bulk material studied here and in a thin film form within a space-restricted area related to a focused laser beam or electric pulse may have different nature, that is, a predominant crystallization of high-pressure phases. We should also mention that in classical and widely used PCMs based on the GeTe–Sb₂Te₃ composition line, all ternary crystalline compounds,^{105,106} including $\text{Ge}_2\text{Sb}_2\text{Te}_5$,

exhibit incongruent melting and hence a dissociation into GaTe and Sb_2Te_3 end members in the melt.¹⁰⁷

Crystallization of high-pressure phases, stable from 4 to 8 GPa, on conventional heating of glasses synthesized under ambient conditions is a very rare, if ever known, phenomenon. In contrast, microtectonics is known in geology since the early 1960s and observed in many silicates.¹⁰⁸ Strong intracrystalline deformation caused by nanotectonic compression was recently reported in natural magnetite and other iron oxides and was found to be consistent with the regional tectonic reference frame.⁵⁸ We use the term “nanotectonic compression” to explain the effect of high internal pressure acting on incipient high-pressure nuclei in metastable viscous and rigid liquid above the crystallization temperature.

A detailed mechanism of nanotectonic compression in supercooled Te-rich liquids is still a subject of further studies. Our hypothesis consists of a substantial difference between the thermal expansion coefficients of a rigid viscous supercooled Ga–Te liquid and incipient nanocrystalline nuclei of tellurium or Ga_2Te_3 . The variable geometry of Te- and Ga-rich domains in liquid $\text{Ga}_{0.2}\text{Te}_{0.8}$, including dense high-pressure motifs of HP-Te II and HP- Ga_2Te_3 (see the two previous sections), facilitates the appearance of HP-related nuclei because of low interfacial free energy at the nucleus/supercooled liquid interface.¹⁰⁹ The growth of high-pressure crystallites is promoted by high interfacial internal pressure arising either as a result of anomalous negative expansion in the supercooled liquid domain, similar to that in supercooled Te,¹¹⁰ or, just in contrast, because of a big difference in linear thermal expansion coefficients for liquid α_L and solid α_S phases (up to $\alpha_L/\alpha_S \cong 7$ in the Ga–Te system).⁵⁹ Consequently, the HP-crystallites are experiencing a strong compression of nanotectonic type from the neighboring rigid supercooled liquid. A schematic representation of this hypothesis is shown in Figure 16. A heterogeneous liquid dynamics and a collective particle motion^{57,111,112} instead of a uniform hydrostatic medium

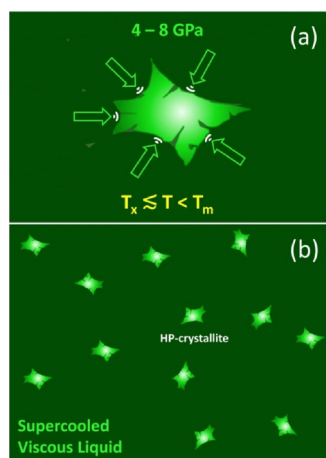


Figure 16. Schematic representation of nanotectonic compression upon heating the glass, which becomes a supercooled, viscous, and rigid Ga–Te liquid: (a) a nanocrystallite nucleus, appearing above the crystallization temperature T_x , is experiencing high internal pressures up to 4–8 GPa at the nanocrystallite/supercooled liquid interface, possibly amplified by a heterogeneous liquid dynamics and (b) a two-phase region containing supercooled viscous liquid and solid high-pressure nanocrystallites frozen on fast cooling from temperatures below the melting point T_m .

would enhance the effect of compression and interfacial transition pressure reaching 4–8 GPa. Finally, a high-pressure HP-allotrope (monoclinic Te-II, $P2_1$) or HP-polymorph (rhombohedral Ga_2Te_3 , $R\bar{3}m$) is formed and frozen after cooling.

Metallic HP-forms, monoclinic Te-II and rhombohedral Ga_2Te_3 , exhibit a much higher conductivity compared to ambient pressure crystals and even more to amorphous forms. The resistivity of monoclinic tellurium decreases by 3 orders of magnitude above 4 GPa,¹¹³ and then Te-II becomes superconducting at 3 K.¹¹⁴ Glassy $\text{Ga}_{0.2}\text{Te}_{0.8}$ transforms into a metallic crystal at 6.5 ± 0.5 GPa, and the conductivity increases by 6 orders of magnitude.¹⁵ Consequently, the frozen HP-forms, presumably emerging after appropriate laser or electric pulses in Ga–Te thin films, appear to be beneficial for PCM performance, increasing optical and electric contrast between the SET and RESET states. A higher contrast also means a lower required energy density producing a distinct step in multilevel information writing, thus decreasing the power consumption.

CONCLUDING REMARKS

Synthesized bulk binary $\text{Ga}_x\text{Te}_{1-x}$ glasses, $0.17 \leq x \leq 0.25$, are characterized by increasing glass transition temperatures, decreasing band-to-band electronic conductivity over the extended states with a typical behavior $E_a \approx 1/2E_g$, where E_a is the conductivity activation energy and E_g is the optical band gap, and a very unusual nanotectonic phenomenon, cocrystallization of high-pressure crystalline polymorphs (typically stable above 4–8 GPa), upon conventional glass heating over the temperature range $T_x \lesssim T < T_m$, where T_x and T_m are the glass crystallization temperature and the melting point (liquidus temperature), respectively.

Raman spectroscopy and high-energy X-ray diffraction supported by first-principles simulations have shown a slightly distorted four-fold gallium local environment in bulk glasses with the tetrahedral fraction $f_{T_4} \approx 0.98$ and a negligible population of under- and over-coordinated Ga species $p_{\text{Ga} \neq 4} \leq 0.01$. The average gallium coordination remains intact with increasing x and temperature but reveals a remarkable T -dependent variability in local configurations. Supercooled (600 K) and metallic (1100 K) $\text{Ga}_{0.2}\text{Te}_{0.8}$ liquids exhibit a reduced tetrahedral fraction and an enhanced population of non-four-fold species.

The tellurium local coordination increases with the Ga content and temperature. Two-thirds of tellurium in glassy $\text{Ga}_{0.2}\text{Te}_{0.8}$ has a two-fold local coordination; the remaining Te species are mostly trigonal. Drastic changes are observed above the glass transition and persist both in supercooled and metallic liquids. The average tellurium coordination increases from $N_{\text{Te}-x} = 2.33 \pm 0.05$ (300 K) to 2.53 ± 0.06 (600–1100 K) with comparable proportions of two-fold and trigonal Te. The fractions of terminal Te_{1F} and four-fold Te_{4F} species explode in liquids, in particular, by a factor of 5–10 for Te_{4F} varieties.

Defect octahedral GaTe_4 and GaTe_5 and Te_{4F} species are forming dense structural motifs in supercooled Ga–Te liquids, reminiscent of high-pressure rhombohedral polymorph HP- Ga_2Te_3 and monoclinic allotrope HP-Te II. These structural motifs facilitate the appearance of HP-nuclei because of low interfacial free energy at the nucleus/supercooled liquid interface. The growth of HP-crystallites is promoted by high

interfacial internal pressure of nanotectonic type arising either as a result of anomalous negative expansion in the supercooled liquid domain, similar to that in supercooled Te, or, just in contrast, because of a big difference in linear thermal expansion coefficients for liquid α_L and solid α_S phases.

Metallic high-pressure forms, monoclinic Te II and rhombohedral Ga₂Te₃, exhibit a much higher conductivity compared to ambient pressure crystals and amorphous alloys. Consequently, the frozen HP-forms, presumably emerging after appropriate laser or electric pulses in Ga–Te thin films, appear to be beneficial for PCM performance, increasing optical and electric contrast between the SET and RESET states. A higher contrast also means a lower energy density producing a distinct step in multilevel information writing, thus decreasing the power consumption.

■ ASSOCIATED CONTENT

SI Supporting Information

The Supporting Information is available free of charge at <https://pubs.acs.org/doi/10.1021/acsami.1c09070>.

Diffraction patterns of Ga–Te samples prepared by mechanical milling, diffraction patterns of the Ga_{0.25}Te_{0.75} sample after in situ diffraction measurements, raw Raman data for bulk glassy Ga_{0.25}Te_{0.75}, structural evolution of the ETH-Ga₂Te₆H₆ cluster during DFT optimization, Gaussian fitting of the X-ray total correlation function for glassy Ga_{0.2}Te_{0.8}, nearest neighbor distributions around two-fold and trigonal Te species, structural references and HP-motifs in supercooled viscous Ga_{0.2}Te_{0.8} at 600 K, orientational order parameter q and $B(\theta)$ distributions of Te–Ga–Te bond angles for GaTe₃ and GaTe₅ entities in liquid Ga_{0.2}Te_{0.8}, optimized DFT geometry of size-limited Ga–Te clusters and Te rings, and supporting references (PDF)

■ AUTHOR INFORMATION

Corresponding Author

Eugene Bychkov – *Laboratoire de Physico-Chimie de l'Atmosphère, Université du Littoral Côte d'Opale, 59140 Dunkerque, France; ILIT RAS–Branch of the FSRC "Crystallography and Photonics" RAS, 140700 Shatura, Moscow Region, Russia; orcid.org/0000-0002-3292-1205; Phone: +33-328-658250; Email: Eugene.Bychkov@univ-littoral.fr; Fax: +33-328-658244*

Authors

Maria Bokova – *Laboratoire de Physico-Chimie de l'Atmosphère, Université du Littoral Côte d'Opale, 59140 Dunkerque, France*

Andrey Tverjanovich – *Institute of Chemistry, St. Petersburg State University, 198504 St. Petersburg, Russia*

Chris J. Benmore – *X-ray Science Division, Advanced Photon Source, Argonne National Laboratory, Argonne, Illinois 60439, United States; orcid.org/0000-0001-7007-7749*

Daniele Fontanari – *Laboratoire de Physico-Chimie de l'Atmosphère, Université du Littoral Côte d'Opale, 59140 Dunkerque, France*

Anton Sokolov – *Laboratoire de Physico-Chimie de l'Atmosphère, Université du Littoral Côte d'Opale, 59140 Dunkerque, France; ILIT RAS–Branch of the FSRC "Crystallography and Photonics" RAS, 140700 Shatura, Moscow Region, Russia*

Maxim Khomenko – *ILIT RAS–Branch of the FSRC "Crystallography and Photonics" RAS, 140700 Shatura, Moscow Region, Russia*

Mohammad Kassem – *Laboratoire de Physico-Chimie de l'Atmosphère, Université du Littoral Côte d'Opale, 59140 Dunkerque, France; orcid.org/0000-0003-0512-0004*

Ilya Ozheredov – *ILIT RAS–Branch of the FSRC "Crystallography and Photonics" RAS, 140700 Shatura, Moscow Region, Russia*

Complete contact information is available at: <https://pubs.acs.org/doi/10.1021/acsami.1c09070>

Author Contributions

The manuscript was written through the contributions of all authors. All authors have given approval to the final version of the manuscript.

Notes

The authors declare no competing financial interest.

■ ACKNOWLEDGMENTS

This work was supported by the Ministry of Science and Higher Education under Agreement no. 075-15-2019-1950, state assignment FSRC "Crystallography and Photonics", Russian Academy of Sciences. The work at the Advanced Photon Source, Argonne National Laboratory, was supported in part by the Office of Basic Energy Sciences, US Department of Energy, under Contract no. DE-AC02-06CH1135. The XRD measurements in part were carried out in the resource center of St. Petersburg State University, "Center for X-ray Diffraction Studies". The FPMD simulations were carried out using the HPC computing resources at Lomonosov Moscow State University and at the ILIT RAS in Shatura (Moscow Region). This work was also granted access to the HPC resources of IDRIS (France) under the allocation 2020-A0090910639 made by Grand Equipement National de Calcul Intensif (GENCI) and to use the CALCULCO computing platform, supported by Service Commun du Système d'Information de l'Université du Littoral Côte d'Opale (SCoSI/ULCO).

■ REFERENCES

- (1) Wuttig, M.; Yamada, N. Phase-Change Materials for Rewriteable Data Storage. *Nat. Mater.* **2007**, *6*, 824–832.
- (2) Raoux, S.; Welnic, W.; Ielmini, D. Phase Change Materials and Their Application to Nonvolatile Memories. *Chem. Rev.* **2010**, *110*, 240–267.
- (3) Kolobov, A. V.; Tominaga, J. *Chalcogenides: Metastability and Phase Change Phenomena*; Springer: Berlin, 2012; pp 149–216.
- (4) Ríos, C.; Stegmaier, M.; Hosseini, P.; Wang, D.; Scherer, T.; Wright, C. D.; Bhaskaran, H.; Pernice, W. H. P. Integrated All-Photonic Non-Volatile Multi-Level Memory. *Nat. Photonics* **2015**, *9*, 725–732.
- (5) Zhang, W.; Mazzarello, R.; Wuttig, M.; Ma, E. Designing Crystallization in Phase-Change Materials for Universal Memory and Neuro-Inspired Computing. *Nat. Rev. Mater.* **2019**, *4*, 150–168.
- (6) Dragoni, D.; Gabardi, S.; Bernasconi, M. First-Principles Study of the Liquid and Amorphous Phases of In₂Te₃. *Phys. Rev. Mater.* **2017**, *1*, No. 035603.
- (7) Sun, L.; Zhou, Y.-X.; Wang, X.-D.; Chen, Y.-H.; Deringer, V. L.; Mazzarello, R.; Zhang, W. Ab Initio Molecular Dynamics and Materials Design for Embedded Phase-Change Memory. *NPJ Comput. Mater.* **2021**, *7*, No. 29.
- (8) Zhang, L.; Mai, X.; Gu, R.; Liu, L.; Xiong, C.; Yang, Z.; Tong, H.; Cheng, X.; Xu, M.; Zhou, P.; Miao, X. Three Resistance States

Achieved by Nanocrystalline Decomposition in Ge-Ga-Sb Compound for Multilevel Phase Change Memory. *Adv. Electron. Mater.* **2021**, *7*, No. 2100164.

(9) Zhu, H.; Yin, J.; Xia, Y.; Liu, Z. Ga₂Te₃ Phase Change Material for Low-Power Phase Change Memory Application. *Appl. Phys. Lett.* **2010**, *97*, No. 083504.

(10) Lee, D.; Kim, T.; Sohn, H. Highly Reliable Threshold Switching Behavior of Amorphous Ga₂Te₃ Films Deposited by RF Sputtering. *Appl. Phys. Express* **2019**, *12*, No. 085504.

(11) Luo, H. L.; Duwez, P. Metastable Amorphous Phases in Tellurium-Base Alloys. *Appl. Phys. Lett.* **1963**, *2*, No. 21.

(12) Cornet, J. The Eutectic Law for Binary Te-Based Systems: A Correlation Between Glass Formation and Eutectic Composition. In *Structure and Properties of Non-Crystalline Semiconductors*; Kolomiets, B. T., Eds.; Nauka: Leningrad, 1976; pp 72–77.

(13) Prasad, M. V. N.; Asokan, S.; Parthasarathy, G.; Titus, S. S. K.; Gopal, E. S. R. Thermal Crystallization Studies on Ga-Te Glasses. *J. Therm. Anal.* **1995**, *44*, 583–587.

(14) Clavaguera, N.; Clavaguera-Mora, M. T.; Fontana, M. Accuracy in the Experimental Calorimetric Study of the Crystallization Kinetics and Predictive Transformation Diagrams: Application to a Ga-Te Amorphous Alloy. *J. Mater. Res.* **1998**, *13*, 744–753.

(15) Parthasarathy, G.; Asokan, S.; Titus, S. S. K.; Krishna, R. R. Metallization and crystallization of semiconducting amorphous Ga₂₀Te₈₀ alloy under high pressure. *Phys. Lett. A* **1988**, *131*, 441–444.

(16) Prasad, M. V. N.; Asokan, S.; Parthasarathy, G.; Titus, S. S. K.; Gopal, E. S. R. High Pressure Electrical Resistivity Studies on Ga-Te Glasses. *High Pressure Res.* **1993**, *11*, 195–200.

(17) Bekheet, A. E. Electrical and Optical Properties of Amorphous Ga₂Te₃ Films. *Eur. Phys. J.: Appl. Phys.* **2001**, *16*, 187–193.

(18) Takeda, S.; Tamaki, S.; Waseda, Y. Local Ordering Features in the Structure of Liquid Ga-Te Alloys. *J. Phys. Soc. Jpn.* **1983**, *52*, 2062–2071.

(19) Hoyer, W.; Müller, A.; Matz, W.; Wobst, M. Neutron Scattering Investigation on Molten Ga-Te Alloys. *Phys. Status Solidi A* **1984**, *84*, 11–18.

(20) Buchanan, P.; Barnes, A. C.; Whittle, K. R.; Hamilton, M. A.; Fitch, A. N.; Fischer, H. E. A Determination of the Structure of Liquid Ga₂Te₃ using Combined X-ray Diffraction and Neutron Diffraction with Isotopic Substitution. *Mol. Phys.* **2001**, *99*, 767–772.

(21) Kolobov, A. V.; Fons, P.; Krbal, M.; Mitrofanov, K.; Tominaga, J.; Uruga, T. Local Structure of the Crystalline and Amorphous States of Ga₂Te₃ Phase-Change Alloy without Resonant Bonding: A Combined X-ray Absorption and Ab Initio Study. *Phys. Rev. B* **2017**, *95*, No. 054114.

(22) Hammersley, A. P.; Svensson, S. O.; Hanfland, M.; Fitch, A. N.; Häusermann, D. Two-Dimensional Detector Software: From Real Detector to Idealised Image or Two-Theta Scan. *High Pressure Res.* **1996**, *14*, 235–248.

(23) Skinner, L. B.; Benmore, C. J.; Parise, J. B. Area Detector Corrections for High Quality Synchrotron X-ray Structure Factor Measurements. *Nucl. Instrum. Methods Phys. Res.* **2012**, *662*, 61–70.

(24) Frisch, M. J.; Trucks, G. W.; Schlegel, H. B.; Scuseria, G. E.; Robb, M. A.; Cheeseman, J. R.; Scalmani, G.; Barone, V.; Petersson, G. A.; Nakatsuji, H.; Li, X.; Caricato, M.; Marenich, A. V.; Bloino, J.; Janesko, B. G.; Gomperts, R.; Mennucci, B.; Hratchian, H. P.; Ortiz, J. V.; Izmaylov, A. F.; Sonnenberg, J. L.; Williams-Young, D.; Ding, F.; Lipparini, F.; Egidi, F.; Goings, J.; Peng, B.; Petrone, A.; Henderson, T.; Ranasinghe, D.; Zakrzewski, V. G.; Gao, J.; Rega, N.; Zheng, G.; Liang, W.; Hada, M.; Ehara, M.; Toyota, K.; Fukuda, R.; Hasegawa, J.; Ishida, M.; Nakajima, T.; Honda, Y.; Kitao, O.; Nakai, H.; Vreven, T.; Throssell, K.; Montgomery, J. A.; Peralta, J. E.; Ogliaro, F.; Bearpark, M. J.; Heyd, J. J.; Brothers, E. N.; Kudin, K. N.; Staroverov, V. N.; Keith, T. A.; Kobayashi, R.; Normand, J.; Raghavachari, K.; Rendell, A. P.; Burant, J. C.; Iyengar, S. S.; Tomasi, J.; Cossi, M.; Millam, J. M.; Klene, M.; Adamo, C.; Cammi, R.; Ochterski, J. W.; Martin, R. L.; Morokuma, K.; Farkas, O.; Foresman, J. B.; Fox, D. J. *Gaussian 16*, revision B.01; Gaussian, Inc.: Wallingford, CT, 2016.

(25) Becke, A. D. Density-Functional Thermochemistry. III. The Role of Exact Exchange. *J. Chem. Phys.* **1993**, *98*, 5648–5653.

(26) Lee, C.; Yang, W.; Parr, R. G. Development of the Colle-Salvetti Correlation-Energy Formula into a Functional of the Electron Density. *Phys. Rev. B* **1988**, *37*, No. 785.

(27) Feller, D. The Role of Databases in Support of Computational Chemistry Calculations. *J. Comput. Chem.* **1996**, *17*, 1571–1586.

(28) Peterson, K. A.; Figgen, D.; Goll, E.; Stoll, H.; Dolg, M. Systematically Convergent Basis Sets with Relativistic Pseudopotentials. II. Small-Core Pseudopotentials and Correlation Consistent Basis Sets for the Post-d Group 16–18 Elements. *J. Chem. Phys.* **2003**, *119*, 11113–11123.

(29) Bacskay, G. B. A Quadratically Convergent Hartree-Fock (QCSCF) Method. Application to Closed Shell Systems. *Chem. Phys.* **1981**, *61*, 385–404.

(30) Masselin, P.; Le Coq, D.; Cuisset, A.; Bychkov, E. Spatially Resolved Raman Analysis of Laser Induced Refractive Index Variation in Chalcogenide Glass. *Opt. Mater. Express* **2012**, *2*, 1768–1775.

(31) Tverjanovich, A.; Cuisset, A.; Fontanari, D.; Bychkov, E. Structure of Se-Te Glasses by Raman Spectroscopy and DFT Modelling. *J. Am. Ceram. Soc.* **2018**, *101*, 5188–5197.

(32) Kassem, M.; Bokova, M.; Tverjanovich, A. S.; Fontanari, D.; Le Coq, D.; Sokolov, A.; Masselin, P.; Kohara, S.; Usuki, T.; Hannon, A. C.; Benmore, C. J.; Bychkov, E. Bent HgI₂ Molecules in the Melt and Sulfide Glasses: Implications for Nonlinear Optics. *Chem. Mater.* **2019**, *31*, 4103–4112.

(33) Hutter, J.; Iannuzzi, M.; Schimann, F.; VandeVondele, J. CP2K: Atomistic Simulations of Condensed Matter Systems. *WIREs: Comput. Mol. Sci.* **2014**, *4*, 15–25.

(34) Perdew, J. P.; Ernzerhof, M.; Burke, K. Rationale for Mixing Exact Exchange with Density Functional Approximations. *J. Chem. Phys.* **1996**, *105*, 9982–9985.

(35) Adamo, C.; Barone, V. Toward Reliable Density Functional Methods without Adjustable Parameters: The PBE0 Model. *J. Chem. Phys.* **1999**, *110*, 6158–6170.

(36) Grimme, S.; Ehrlich, S.; Goerigk, L. Effect of the Damping Function in Dispersion Corrected Density Functional Theory. *J. Comput. Chem.* **2011**, *32*, 1456–1465.

(37) Micoulaut, M. Communication: Van der Waals Corrections for an Improved Structural Description of Telluride Based Materials. *J. Chem. Phys.* **2013**, *138*, No. 061103.

(38) Bouzid, A.; Massobrio, C.; Boero, M.; Ori, G.; Sykina, K.; Furet, E. Role of the van der Waals Interactions and Impact of the Exchange-Correlation Functional in Determining the Structure of Glassy GeTe₄. *Phys. Rev. B* **2015**, *92*, No. 134208.

(39) Akola, J.; Jones, R. O.; Kohara, S.; Kimura, S.; Kobayashi, K.; Takata, M.; Matsunaga, T.; Kojima, R.; Yamada, N. Experimentally Constrained Density-Functional Calculations of the Amorphous Structure of the Prototypical Phase-Change Material Ge₂Sb₂Te₅. *Phys. Rev. B* **2009**, *80*, No. 020201.

(40) Matsunaga, T.; Akola, J.; Kohara, S.; Honma, T.; Kobayashi, K.; Ikenaga, E.; Jones, R. O.; Yamada, N.; Takata, M.; Kojima, R. From Local Structure to Nanosecond Recrystallization Dynamics in AgInSbTe Phase-Change Materials. *Nat. Mater.* **2011**, *10*, 129–134.

(41) Gereben, O.; Pusztai, L. RMC_POT, a Computer Code for Reverse Monte Carlo Modeling the Structure of Disordered Systems Containing Molecules of Arbitrary Complexity. *J. Comput. Chem.* **2012**, *33*, 2285–2291.

(42) Hartwigsen, C.; Goedecker, S.; Hutter, J. Relativistic Separable Dual-Space Gaussian Pseudo-potentials from H to Rn. *Phys. Rev. B* **1998**, *58*, No. 3641.

(43) Nosé, S. A Molecular Dynamics Method for Simulations in the Canonical Ensemble. *Mol. Phys.* **1984**, *52*, 255–268.

(44) Hoover, W. G. Canonical Dynamics: Equilibrium Phase-Space Distributions. *Phys. Rev. A* **1985**, *31*, No. 1695.

(45) Le Roux, S.; Jund, P. Ring Statistics Analysis of Topological Networks: New Approach and Application to Amorphous GeS₂ and SiO₂ Systems. *Comput. Mater. Sci.* **2010**, *49*, 70–83.

- (46) Kohara, S.; Ohno, H.; Takata, M.; Usuki, T.; Morita, H.; Suzuya, K.; Akola, J.; Puztai, L. Lead Silicate Glasses: Binary Network-Former Glasses with Large Amounts of Free Volume. *Phys. Rev. B* **2010**, *82*, No. 134209.
- (47) Heimbach, I.; Rhiem, F.; Beule, F.; Knodt, D.; Heinen, J.; Jones, R. O. pyMolDyn: Identification, Structure, and Properties of Cavities/Vacancies in Condensed Matter and Molecules. *J. Comput. Chem.* **2017**, *38*, 389–394.
- (48) Guymont, M.; Tomas, A.; Guittard, M. The Structure of Ga_2Te_3 . An X-ray and High-Resolution Electron Microscopy Study. *Philos. Mag. A* **1992**, *66*, 133–139.
- (49) Chérin, P.; Unger, P. Two-Dimensional Refinement of the Crystal Structure of Tellurium. *Acta Crystallogr.* **1967**, *23*, 670–671.
- (50) Julien-Pouzol, M.; Jaulmes, S.; Alapini, F. Tellurure de Gallium. *Acta Crystallogr. B* **1977**, *33*, 2270–2272.
- (51) Deiseroth, H. J.; Amann, P.; Thurn, H. Die Pentatelluride M_2Te_5 (M = Al, Ga, In): Polymorphie, Strukturbeziehungen und Homogenitätsbereiche. *Z. Anorg. Allg. Chem.* **1996**, *622*, 985–993.
- (52) Fontana, M.; Arcondo, B.; Clavaguera-Mora, M. T.; Clavaguera, N. Mechanisms Controlling Primary Crystallisation of $\text{Ga}_{20}\text{Te}_{80}$ glasses. *J. Non-Cryst. Solids* **2007**, *353*, 2131–2142.
- (53) Aoki, K.; Shimomura, O.; Minomura, S. Crystal Structure of the High-Pressure Phase of Tellurium. *J. Phys. Soc. Jpn.* **1980**, *48*, 551–556.
- (54) Takumi, M.; Masamitsu, T.; Nagata, K. X-Ray Structural Analysis of the High-Pressure Phase III of Tellurium. *J. Phys.: Condens. Matter* **2002**, *14*, 10609–10613.
- (55) Serebryanaya, N. R. The Crystal Structure of Pressure-Induced Phases of In_2Te_3 and Ga_2Te_3 . *Powder Diffr.* **1992**, *7*, 99–102.
- (56) Davis, S. A.; Breulmann, M.; Rhodes, K. H.; Zhang, B.; Mann, S. Template-Directed Assembly Using Nanoparticle Building Blocks: A Nanotectonic Approach to Organized Materials. *Chem. Mater.* **2001**, *13*, 3218–3226.
- (57) Zhang, H.; Douglas, J. F. Glassy Interfacial Dynamics of Ni Nanoparticles: Part II. Discrete Breathers as an Explanation of Two-Level Energy Fluctuations. *Soft Matter* **2013**, *9*, 1266–1280.
- (58) Mamtani, M. A.; Reznik, B.; Kontny, A. Intracrystalline Deformation and Nanotectonic Processes in Magnetite from a Naturally Deformed Rock. *J. Struct. Geol.* **2020**, *135*, No. 104045.
- (59) Glazov, V. M.; Chizhevskaya, S. N.; Glagoleva, N. N. *Liquid Semiconductors*; Plenum: New York, 1969; pp 142–150, 317–333. Glazov, V. M.; Chizhevskaya, S. N.; Glagoleva, N. N. *Liquid Semiconductors (Zhidkie Poluprovodniki)*; Nauka: Moscow, 1967; pp 194–196, 215–230.
- (60) Popp, K.; Tschirner, H.-U.; Wobst, M. Electrical Conductivity and Thermoelectric Power of Liquid In-Te Alloys. *Philos. Mag.* **1974**, *30*, 685–690.
- (61) Tschirner, H.-U.; Uhlig, K.; Wobst, M. Hall Coefficient of Liquid Ga-Te Alloys. *Philos. Mag. B* **1984**, *50*, 645–655.
- (62) Ray, A. K.; Swan, R.; Hogarth, C. A. Conduction Mechanisms in Amorphous Tellurium Films. *J. Non-Cryst. Solids* **1994**, *168*, 150–156.
- (63) Skal, A. S.; Andreev, A. A.; Tschirner, H.-U. Percolation Theory and Transport Coefficients in Disordered Systems. *Philos. Mag. B* **1982**, *45*, 323–333.
- (64) Mott, N. F.; Davis, E. A. *Electronic Processes in Non-Crystalline Materials*, 2nd ed.; Clarendon Press: Oxford, 1979; pp 5–64, 272–300.
- (65) Hilton, A. R. *Chalcogenide Glasses for Infrared Optics*; McGraw-Hill: New York, 2010; pp 1–15.
- (66) Sanghera, J.; Gibson, D. Optical Properties of Chalcogenide Glasses and Fibers. In *Chalcogenide Glasses: Preparation, Properties and Applications*; Adam, J.-L., Zhang, X., Eds.; Woodhead Publishing: Oxford, 2014; pp 113–138.
- (67) Le Coq, D.; Cui, S.; Boussard-Plédel, C.; Masselin, P.; Bychkov, E.; Bureau, B. Telluride glasses with far-infrared transmission up to 35 μm . *Opt. Mater.* **2017**, *72*, 809–812.
- (68) Moss, T. S. Relations between the Refractive Index and Energy Gap of Semiconductors. *Phys. Status Solidi* **1985**, *131*, 415–427.
- (69) Stuke, J. Review of Optical and Electrical Properties of Amorphous Semiconductors. *J. Non-Cryst. Solids* **1970**, *4*, 1–26.
- (70) Popescu, M.; Sava, F.; Lőrinczi, A.; Velea, A.; Simandan, I. D.; Galca, A. C.; Matei, E.; Socol, G.; Gherendi, F.; Savastru, D.; Miclos, S. Amorphous thin films in the gallium–chalcogen system. *Phys. Status Solidi B* **2016**, *253*, 1033–1037.
- (71) Tauc, J. Optical Properties of Amorphous Semiconductors. In *Amorphous and Liquid Semiconductors*; Tauc, J., Eds.; Plenum: London, 1974; pp 159–220.
- (72) Brodsky, M. H.; Gambino, R. J.; Smith, J. E., Jr.; Yacoby, Y. The Raman Spectrum of Amorphous Tellurium. *Phys. Status Solidi* **1972**, *52*, 609–614.
- (73) Tverjanovich, A.; Rodionov, K.; Bychkov, E. Raman Spectroscopy of Glasses in the As–Te System. *J. Solid State Chem.* **2012**, *190*, 271–276.
- (74) Tverjanovich, A.; Khomenko, M.; Benmore, C. J.; Bokova, M.; Sokolov, A.; Fontanari, D.; Kassem, M.; Usuki, T.; Bychkov, E. Bulk Glassy GeTe_2 : A Missing Member of the Tetrahedral GeX_2 Family and a Precursor for the Next Generation of Phase-Change Materials. *Chem. Mater.* **2021**, *33*, 1031–1045.
- (75) Deiseroth, H. J.; Wagener, M.; Neumann, E. $(\text{AgI})_2\text{Te}_6$ and $(\text{AgI})_2\text{Se}_6$: New Composite Materials with Cyclic Te_6 and Se_6 Molecules Stabilized in the “Solid Solvent” AgI . *Eur. J. Inorg. Chem.* **2004**, *2004*, 4755–4758.
- (76) Sheldrick, W. S.; Wachhold, M. Discrete Crown-Shaped Te_8 Rings in $\text{Cs}_3\text{Te}_{22}$. *Angew. Chem., Int. Ed.* **1995**, *34*, 450–451.
- (77) Günther, A.; Isaeva, A.; Baranov, A. I.; Ruck, M. Neutral Tellurium Rings in the Coordination Polymers $[\text{Ru}(\text{Te}_9)](\text{InCl}_4)_2$, $[\text{Ru}(\text{Te}_8)]\text{Cl}_2$, and $[\text{Rh}(\text{Te}_6)]\text{Cl}_3$. *Chem. Eur. J.* **2011**, *17*, 6382–6388.
- (78) Betts, F.; Bienenstock, A.; Ovshinsky, S. R. Radial Distribution Studies of Amorphous $\text{Ge}_x\text{Te}_{1-x}$ Alloys. *J. Non-Cryst. Solids* **1970**, *4*, 554–563.
- (79) Uemura, O.; Hayasaka, N.; Tokairin, S.; Usuki, T. Local Atomic Arrangement in Ge-Te and Ge-S-Te Glasses. *J. Non-Cryst. Solids* **1996**, *205–207*, 189–193.
- (80) Kaban, I.; Th, H.; Hoyer, W.; Jóvári, P.; Neufeind, J. Short-range order in amorphous germanium–tellurium alloys. *J. Non-Cryst. Solids* **2003**, *326–327*, 120–124.
- (81) Kalikka, J.; Akola, J.; Jones, R. O.; Kohara, S.; Usuki, T. Amorphous $\text{Ge}_{15}\text{Te}_{85}$: Density Functional, High-Energy X-ray and Neutron Diffraction Study. *J. Phys.: Condens. Matter* **2012**, *24*, No. 015802.
- (82) Wei, S.; Stolpe, M.; Gross, O.; Hembree, W.; Hechler, S.; Bednarcik, J.; Busch, R.; Lucas, P. Structural evolution on medium-range-order during the fragile-strong transition in $\text{Ge}_{15}\text{Te}_{85}$. *Acta Mater.* **2017**, *129*, 259–267.
- (83) Voleská, I.; Akola, J.; Jóvári, P.; Gutwirth, J.; Wágner, T.; Vasileiadis, T.; Yannopoulos, S. N.; Jones, R. O. Structure, Electronic, and Vibrational Properties of Glassy $\text{Ga}_{11}\text{Ge}_{11}\text{Te}_{78}$: Experimentally Constrained Density Functional Study. *Phys. Rev. B* **2012**, *86*, No. 094108.
- (84) Pethes, I.; Piarristeguy, A.; Pradel, A.; Michalik, S.; Nemausat, R.; Darpentigny, J.; Jóvári, P. Short Range Order and Topology of $\text{Ge}_x\text{Ga}_x\text{Te}_{100-2x}$ Glasses. *J. Alloys Compd.* **2020**, *834*, No. 155097.
- (85) Lorch, E. Neutron Diffraction by Germania, Silica and Radiation-Damaged Silica Glasses. *J. Phys. C: Solid State Phys.* **1969**, *2*, 229–237.
- (86) Julien-Pouzol, M.; Jaulmes, S.; Guittard, M.; Alapini, F. Monotellurure de Gallium, GaTe . *Acta Crystallogr. B* **1979**, *35*, 2848–2851.
- (87) Ichikawa, T. Electron Diffraction Study of the Local Atomic Arrangement in Amorphous Tellurium Films. *Phys. Status Solidi* **1973**, *56*, 707–715.
- (88) Kassem, M.; Bounazef, T.; Fontanari, D.; Sokolov, A.; Bokova, M.; Hannon, A. C.; Bychkov, E. Chemical and Structural Variety in Sodium Thioarsenate Glasses Studied by Neutron Diffraction and Supported by First-Principles Simulations. *Inorg. Chem.* **2020**, *59*, 16410–16420.

- (89) Tverjanovich, A.; Khomenko, M.; Bereznev, S.; Fontanari, D.; Sokolov, A.; Usuki, T.; Ohara, K.; Le Coq, D.; Masselin, P.; Bychkov, E. Glassy GaS: Transparent and Unusually Rigid Thin Films for Visible to Mid-IR Memory Applications. *Phys. Chem. Chem. Phys.* **2020**, *22*, 25560–25573.
- (90) Deiseroth, H. J.; Müller, H.-D. Crystal Structures of Heptagallium Decatelluride, Ga₇Te₁₀ and Heptaindium Decatelluride, In₇Te₁₀. *Z. Kristallogr.* **1995**, *210*, 57–58.
- (91) Chau, P.-L.; Hardwick, A. J. A New Order Parameter for Tetrahedral Configurations. *Mol. Phys.* **1998**, *93*, 511–518.
- (92) Errington, J. R.; Debenedetti, P. G. Relationship between Structural Order and the Anomalies of Liquid Water. *Nature* **2001**, *409*, 318–321.
- (93) Akola, J.; Jones, R. O.; Kohara, S.; Usuki, T.; Bychkov, E. Density Variations in Liquid Tellurium: Roles of Rings, Chains, and Cavities. *Phys. Rev. B* **2010**, *81*, No. 094202.
- (94) Akola, J.; Jones, R. O. Structure and Dynamics in Amorphous Tellurium and Ten Clusters: A Density Functional Study. *Phys. Rev. B* **2012**, *85*, No. 134103.
- (95) Qiao, C.; Xu, M.; Wang, S.; Wang, C.-Z.; Ho, K.-M.; Miao, X.; Xu, M. Structure, Bonding Nature and Transition Dynamics of Amorphous Te. *Scr. Mater.* **2021**, *202*, No. 114011.
- (96) Akola, J.; Jones, R. O. Binary Alloys of Ge and Te: Order, Voids, and the Eutectic Composition. *Phys. Rev. Lett.* **2008**, *100*, No. 205502.
- (97) Caravati, S.; Bernasconi, M.; Parrinello, M. First-Principles Study of Liquid and Amorphous Sb₂Te₃. *Phys. Rev. B* **2010**, *81*, No. 014201.
- (98) Song, J.-W.; Giorgi, G.; Yamashita, K.; Hirao, K. Communication: Singularity-Free Hybrid Functional with a Gaussian-Attenuating Exact Exchange in a Plane-Wave Basis. *J. Chem. Phys.* **2013**, *138*, No. 241101.
- (99) Flores-Ruiz, H.; Micoulaut, M.; Piarristeguy, A.; Coulet, M.-V.; Johnson, M.; Cuello, G. J.; Pradel, A. Structural, Vibrational, and Dynamic Properties of Ge-Ga-Te Liquids with Increasing Connectivity: A Combined Neutron Scattering and Molecular Dynamics Study. *Phys. Rev. B* **2018**, *97*, No. 214207.
- (100) Dragoni, D.; Bernasconi, M. Structural and Electronic Properties of Liquid, Amorphous and Supercooled Liquid Phases of In₂Te₃ from First-Principles. *J. Chem. Phys.* **2019**, *151*, No. 134503.
- (101) Micoulaut, M.; Coulet, M.-V.; Piarristeguy, A. A.; Johnson, M. R.; Cuello, G. J.; Bichara, C.; Raty, J.-Y.; Flores-Ruiz, H.; Pradel, A. Effect of Concentration in Ge-Te Liquids: A Combined Density Functional and Neutron Scattering Study. *Phys. Rev. B* **2014**, *89*, No. 174205.
- (102) Raty, J. Y.; Zhang, W.; Luckas, J.; Chen, C.; Mazzarello, R.; Bichara, C.; Wuttig, M. Aging Mechanisms in Amorphous Phase-Change Materials. *Nat. Commun.* **2015**, *6*, No. 7467.
- (103) Jóvári, P.; Piarristeguy, A.; Escalier, R.; Kaban, I.; Bednarčík, J.; Pradel, A. Short Range Order and Stability of Amorphous Ge_xTe_{100-x} Alloys (12 ≤ x ≤ 44.6). *J. Phys.: Condens. Matter* **2013**, *25*, No. 195401.
- (104) Chang-Seok, O.; Nyung, L. D. Thermodynamic Assessment of the Ga-Te System. *CALPHAD* **1992**, *16*, 317–330.
- (105) Abrikosov, N. K.; Danilova-Dobryakova, G. T. Sb₂Te₃-GeTe Phase Diagram. *Izv. Akad. Nauk SSSR: Neorg. Mater.* **1965**, *1*, 204–209.
- (106) Shelimova, L. E.; Karpinskii, O. G.; Konstantinov, P. P.; Kretova, M. A.; Avilov, E. S.; Zemskov, V. S. Composition and Properties of Layered Compounds in the GeTe-Sb₂Te₃ System. *Inorg. Mater.* **2001**, *37*, 342–348.
- (107) Boniardi, M. Thermal Model and Remarkable Temperature Effects on the Chalcogenide Alloy. In *Phase Change Memory: Device Physics, Reliability and Applications*; Redaelli, A., Ed.; Springer: Cham, Switzerland, 2018; pp 41–64.
- (108) Passchier, C. W.; Trouw, R. A. J. *Microtectonics*, 2nd ed.; Springer: Berlin, 2005; pp 56–66.
- (109) Turnbull, D.; Fisher, J. C. Rate of Nucleation in Condensed Systems. *J. Chem. Phys.* **1949**, *17*, 71–73.
- (110) Tsuchiya, Y. Thermodynamic Evidence for a Structural Transition of Liquid Te in the Supercooled Region. *J. Phys. Condens. Matter.* **1991**, *3*, 3163–3172.
- (111) Glotzer, S. C. Spatially Heterogeneous Dynamics in Liquids: Insights from Simulation. *J. Non-Cryst. Solids* **2000**, *274*, 342–355.
- (112) Sosso, G. C.; Colombo, J.; Behler, J.; Del Gado, E.; Bernasconi, M. Dynamical Heterogeneity in the Supercooled Liquid State of the Phase Change Material GeTe. *J. Phys. Chem. B* **2014**, *118*, 13621–13628.
- (113) Bridgman, P. W. The Resistance of 72 Elements, Alloys and Compounds to 100,000 kg/cm². *Proc. Am. Acad. Arts Sci.* **1952**, *81*, 165–251.
- (114) Matthias, B. T.; Olsen, J. L. Superconductivity of Tellurium. *Phys. Lett.* **1964**, *13*, 202–203.